



Publication Year	2019
Acceptance in OA@INAF	2021-04-23T09:41:02Z
Title	On a New Method to Estimate the Distance, Reddening, and Metallicity of RR p̃ Lyrae Stars Using Optical/Near-infrared (B, V, I, J, H Centauri as a First Test Case
Authors	Bono, G.; Iannicola, G.; Braga, Vittorio Francesco; Ferraro, I.; Stetson, P. B.; et al.
DOI	10.3847/1538-4357/aaf23f
Handle	http://hdl.handle.net/20.500.12386/30871
Journal	THE ASTROPHYSICAL JOURNAL
Number	870



On a New Method to Estimate the Distance, Reddening, and Metallicity of RR Lyrae Stars Using Optical/Near-infrared (B , V , I , J , H , K) Mean Magnitudes: ω Centauri as a First Test Case

G. Bono^{1,2}, G. Iannicola², V. F. Braga^{3,4}, I. Ferraro², P. B. Stetson⁵, D. Magurno¹, N. Matsunaga⁶, R. L. Beaton⁷, R. Buonanno⁸, B. Chaboyer⁹, M. Dall’Ora¹⁰, M. Fabrizio^{2,11}, G. Fiorentino¹², W. L. Freedman^{7,13}, C. K. Gilligan⁹, B. F. Madore⁷, M. Marconi¹⁰, M. Marengo¹⁴, S. Marinoni^{2,11}, P. M. Marrese^{2,11}, C. E. Martinez-Vazquez¹⁵, M. Mateo¹⁶, M. Monelli^{17,18}, J. R. Neeley¹⁹, M. Nonino²⁰, C. Sneden²¹, F. Thevenin²², E. Valenti²³, and A. R. Walker¹⁵

¹ Department of Physics, Università di Roma Tor Vergata, via della Ricerca Scientifica 1, I-00133 Roma, Italy

² INAF-Osservatorio Astronomico di Roma, via Frascati 33, I-00040 Monte Porzio Catone, Italy

³ Instituto Milenio de Astrofísica, Santiago, Chile

⁴ Departamento de Física, Facultad de Ciencias Exactas, Universidad Andres Bello, Fernandez Concha 700, Las Condes, Santiago, Chile

⁵ NRC-Herzberg, Dominion Astrophysical Observatory, 5071 West Saanich Road, Victoria BC V9E 2E7, Canada

⁶ Kiso Observatory, Institute of Astronomy, School of Science, The University of Tokyo, 10762-30, Mitake, Kisomachi, Kisogun, 3 Nagano 97-0101, Japan

⁷ The Observatories of the Carnegie Institution for Science, 813 Santa Barbara Street, Pasadena, CA 91101, USA

⁸ INAF-Osservatorio Astronomico d’Abruzzo, Via Mentore Maggini snc, Loc. Collurania, I-64100 Teramo, Italy

⁹ Department of Physics and Astronomy, Dartmouth College, Hanover, NH 03755, USA

¹⁰ INAF-Osservatorio Astronomico di Capodimonte, Salita Moiariello 16, I-80131 Napoli, Italy

¹¹ SSDC, via del Politecnico snc, I-00133 Roma, Italy

¹² INAF-Osservatorio di Astrofisica e Scienza dello Spazio di Bologna, Via Piero Gobetti 93/3, I-40129, Bologna, Italy

¹³ Department of Astronomy and Astrophysics, University of Chicago, 5640 S. Ellis Avenue, Chicago, IL 60637, USA

¹⁴ Department of Physics and Astronomy, Iowa State University, Ames, IA 50011, USA

¹⁵ Cerro Tololo Inter-American Observatory, National Optical Astronomy Observatory, Casilla 603, La Serena, Chile

¹⁶ Department of Astronomy, University of Michigan, 1085 S. University, Ann Arbor, MI 48109, USA

¹⁷ Instituto de Astrofísica de Canarias, Calle Via Lactea s/n, E-38205 La Laguna, Tenerife, Spain

¹⁸ Departamento de Astrofísica, Universidad de La Laguna, Tenerife, Spain

¹⁹ Department of Physics, Florida Atlantic University, Boca Raton, FL 33431, USA

²⁰ INAF-Osservatorio Astronomico di Trieste, Via G.B. Tiepolo, 11, I-34143 Trieste, Italy

²¹ Department of Astronomy and McDonald Observatory, The University of Texas, Austin, TX 78712, USA

²² Universite de Nice Sophia-antipolis, CNRS, Observatoire de la Cote d’Azur, Laboratoire Lagrange, BP 4229, F-06304 Nice, France

²³ European Southern Observatory, Karl-Schwarzschild-Str. 2, D-85748 Garching bei Munchen, Germany

Received 2018 September 22; revised 2018 November 16; accepted 2018 November 16; published 2019 January 15

Abstract

We developed a new approach to provide accurate estimates of the metal content, reddening, and true distance modulus of RR Lyrae stars (RRLs). The method is based on homogeneous optical (BVI) and near-infrared (JHK) mean magnitudes and on predicted period–luminosity–metallicity relations (IJK) and absolute mean magnitude–metallicity relations (BV). We obtained solutions for three different RRL samples in ω Cen: first overtone (RRc, 90), fundamental (RRab, 80), and global (RRc+RRab) in which the period of first overtones were fundamentalized. The metallicity distribution shows a well defined peak at $[\text{Fe}/\text{H}] \sim -1.98$ and a standard deviation of $\sigma = 0.54$ dex. The spread is, as expected, metal-poor ($[\text{Fe}/\text{H}] \leq -2.3$) objects. The current metallicity distribution is ~ 0.3 dex more metal-poor than similar estimates for RRLs available in the literature. The difference vanishes if the true distance modulus we estimated is offset by $-0.06/-0.07$ mag in true distance modulus. We also found a cluster true distance modulus of $\mu = 13.720 \pm 0.002 \pm 0.030$ mag, where the former error is the error on the mean and the latter is the standard deviation. Moreover, we found a cluster reddening of $E(B - V) = 0.132 \pm 0.002 \pm 0.028$ mag and spatial variations of the order of a few arcmin across the body of the cluster. Both the true distance modulus and the reddening are slightly larger than similar estimates available in the literature, but the difference is within 1σ . The metallicity dependence of distance diagnostics agrees with theory and observations, but firm constraints require accurate and homogeneous spectroscopic measurements.

Key words: globular clusters: individual (Centauri) – stars: distances – stars: horizontal-branch – stars: variables: RR Lyrae

1. Introduction

The use of RR Lyrae and classical Cepheids as first rungs in the cosmic distance scale dates back to more than one century ago (Leavitt 1908; Hubble 1925; Shapley 1953; Baade 1956). Fundamental contributions on the diagnostics adopted to estimate individual distances have been provided over more than half a century by Sandage & Tammann (1968) and Tammann et al. (2003). The empirical scenario was complemented during the eighties with the use of near-infrared mean

magnitudes by Longmore et al. (1986), Welch et al. (1983), and Madore et al. (1987).

The theoretical framework after the seminal investigations by Cox, Christy, Iben and Castor lagged until a proper treatment for the convective transport (Stellingwerf 1982a, 1982b) was included in the calculation of radial pulsation models. The use of the new radiative and molecular opacities (OP, OPAL), together with a more formal treatment of the free parameters adopted for dealing with eddy viscosity and

artificial viscosity (Bono & Stellingwerf 1994) paved the way to detailed and homogeneous predictions for radial variables in the Cepheid instability strip (Kovacs et al. 1990; Bono et al. 1999; Feuchtinger 1999; Smolec et al. 2013). The key advantage of the latter approach compared with the classical one is the opportunity to constrain the modal stability and the pulsation amplitudes. Moreover, and even more importantly, the use of a common environment between evolutionary and pulsation prescriptions provided for the first time the opportunity to constrain the metallicity dependence of the diagnostics adopted to determine individual distances.

In this context cluster RR Lyrae have played a crucial role, as their progenitors typically share the same ages and the same chemical composition distributions. Moreover, they can be adopted to determine both the zero-point and the slope of optical (R , I , Braga et al. 2016, hereinafter BR16) and near-infrared (NIR, J , H , K , Braga et al. 2018, hereinafter BR18) Period–Luminosity–Metallicity (PLZ) relations. These are key advantages when compared with field variables, because accurate metal abundances are only available for ~ 100 objects (e.g., For et al. 2011; Pancino et al. 2015; Sneden et al. 2017; M. Fabrizio et al. 2018, in preparation). Among the clusters hosting a sizable sample of RRLs, we will focus our attention on ω Cen (NGC 5139) for the following reasons:

- Sample size— ω Cen includes ≈ 200 RRLs that are almost equally split between fundamental and first overtone pulsators (Navarrete et al. 2017, BR18).
- Spread in iron abundance—the current evidence indicates that RRLs in ω Cen cover a range in metallicity of at least one dex: $-2.2 \lesssim [\text{Fe}/\text{H}] \lesssim -1$, (Sollima et al. 2006); $-2.4 \lesssim [\text{Fe}/\text{H}] \lesssim -0.8$, (Rey et al. 2000).
- Mean magnitudes—our group provided a complete census of RRLs in ω Cen (BR16, BR18); this means new and homogeneous optical and NIR mean magnitudes together with the characterization of individual variables (luminosity amplitudes, periods, nonlinear phenomena (mixed-mode, Blazhko)).
- Reddening variation—There is mounting evidence that the cluster is affected by differential reddening (Calamida et al. 2005).

These are the reasons why the quoted optical/NIR data have already been adopted to estimate the cluster distance (BR16, BR18) and the metallicity distribution of RR Lyrae (BR16). To overcome uncertainties on individual metal abundances and extinctions, BR16 evaluated the cluster distance using V , $B - V$ and V , $B - I$ Period–Wesenheit (PW) relations. These relations are, by construction, independent of uncertainties affecting cluster reddening and by the possible presence of differential reddening (Marconi et al. 2015). Moreover, their dependence on metallicity is small (< 0.1 mag/dex) and they can be considered as metal-independent PW relations. A similar approach was adopted by BR18, but the cluster distance was evaluated using NIR (JHK) mean magnitudes that are one order of magnitude less affected by uncertainties on individual reddening when compared with optical mean magnitudes. Moreover, they used the metal abundances available in the literature based either on spectroscopy (Sollima et al. 2006) or on photometric indices (Rey et al. 2000, BR16).

To overcome some of the quoted limitations we introduce a novel approach based on six (B , V , I , J , H , K) mean magnitudes to provide distance, reddening, and metal abundance estimates of

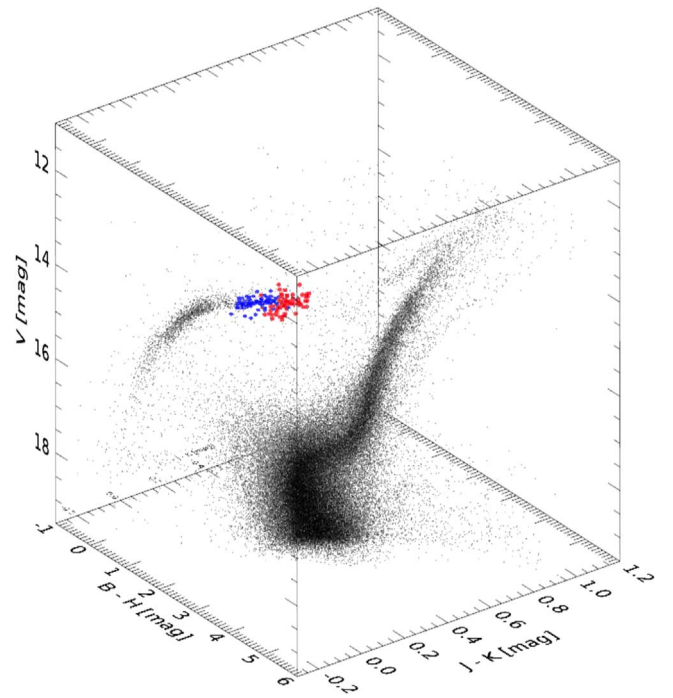


Figure 1. 3D apparent CMD— V , $B - H$, $J - K$ —of ω Cen based on optical and NIR photometry provided by BR16 and BR18. The red and blue circles display the position in the instability strip of both fundamental (RRab) and first overtone (RRc) RRLs. The error on the mean magnitude is typically smaller than the symbol size. The black dots display ω Cen stars selected according to radial distance ($5 \leq r \leq 15$ arcmin) and number of measurements (dozen per band). Only stars brighter than $V = 19.5$ mag were plotted.

individual RRLs. The structure of the paper is as follows. In Section 2 we introduce the empirical and the theoretical frameworks on which this investigation relies. In Section 3 we discuss in detail the new approach we developed to provide homogeneous estimates of metal content, true distance modulus, and reddening of individual RRLs. In particular, we discuss the different steps and assumptions we followed in the first and in second iteration of the method. Section 4 deals with the tests we performed to validate the new approach. In Section 5 we discuss the comparison with similar estimates available in the literature. In particular, the comparison with spectroscopic and spectrophotometric metallicity distributions is discussed in Section 5.1, while Section 5.2 details the reddening distribution and Section 5.3 details the true distance modulus distribution. Finally, Section 6 gives a summary of the current results together with a few remarks concerning the future developments of this project.

2. Empirical and Theoretical Framework

The optical–NIR data adopted in the current investigations are shown in Figure 1. The 3D (V , $B - H$, $J - K$) color–magnitude diagram (CMD) displays a small fraction of cluster stars (black dots) and the position of the entire sample of 196 RRLs. The blue circles display first overtones (RRc), while the red circles show the fundamentals (RRab). The reader interested in the complete census of RRLs concerning candidate Blazhko RRLs and the candidate mixed mode RRL is referred to BR16.

The period–luminosity (PL) and the period–Wesenheit relations adopted in this paper rely on the grid of nonlinear, convective pulsation models computed by Marconi et al. (2015).

The main difference is that the same models were transformed into the observational plane using the very same *JHK* passbands adopted by the 2MASS NIR photometric system.²⁴ This means that we did not use the transformations provided by Campbell et al. (2010) to move from the Bessell & Brett photometric system into the 2MASS system. The new NIR distance diagnostics will be provided in a forthcoming paper (M. Marconi et al. 2018, in preparation).

It is quite well known that RRLs in the bluer optical (*BV*) bands obey a mean magnitude–metallicity relation, while the PL relation becomes more evident for wavelengths longer than the *R* band (Bono et al. 2003; Catelan et al. 2004; Braga et al. 2015; Marconi et al. 2015). To fully exploit the optical data set we also derived new *B* and *V* mean magnitude–metallicity relations. They are based on the same set of RRL models used by Marconi et al. (2015) and will be provided in M. Marconi et al. (2018, in preparation).

3. REDIME: a New Approach to Estimate the REddening, DIstance, and METallicity of RRLs

We developed a new approach to estimate REddening, DIstance modulus and METallicity (REDIME) of field and cluster RRLs. REDIME is only based on optical and NIR measurements, but it can be easily extended to near-UV and mid-infrared bands. The RRLs hosted by ω Cen are roughly 200 and our group collected during the last 15 yr sizable samples of optical (*UBVRI*) and NIR (*JHK*) time series (BR16, BR18). In spite of this unprecedented observational effort there are still RRLs for which either the optical and/or the NIR mean magnitudes are not very accurate. These objects are typically located in the outskirts of the cluster. To avoid possible systematics in applying REDIME we restricted the sample to the RRLs for which we have accurate optical and NIR mean magnitudes. This means variables with good coverage of the light curve and at least 10 phase points per band. We ended up with a sample of 170 RRLs, listed in Table 1. Among them, 90 are RRc and 80 are RRab. Note that the sample also includes 26 candidate Blazhko RRLs. There is only one candidate mixed-mode RRL in ω Cen (Braga et al. 2018) and it was not included in the current analysis. The properties of this interesting RRL variable will be addressed in a separate paper (V. F. Braga et al. 2018, in preparation). The REDIME algorithm relies on two iterations. The former one is aimed at providing an initial homogeneous estimate of the metallicity, true distance modulus, and reddening estimates. The latter is used to further improve both the precision and the accuracy of the initial guess. The individual steps performed to approach the final solution are summarized in the following. The reader interested in a more detailed description of the algorithm is referred to the flow chart presented in the Appendix (see Figure 14) to this paper.

First Iteration: (a)—we provided a new estimate of the cluster distance using the predicted (*V*, *B* – *I*) PW relation. We adopted this relation, since it is independent of reddening uncertainties by construction. Moreover, theory and observations indicate that the metallicity dependence is negligible, and indeed the coefficient of the metallicity term is smaller than 0.1 dex. Furthermore, the standard deviation of this PW relation is

smaller than the other optical (*V*, *B* – *V*) PW relations with a small coefficient of the metallicity term (Marconi et al. 2015).

(b)—we provided a new estimate of the individual metallicities by inverting, using the new mean distance modulus and the mean cluster reddening ($E(B - V) = 0.11$ mag Calamida et al. 2005), four different optical/NIR (*I*, *J*, *H*, *K*) PLZ relations. The same approach, but only based on the *I* band, was already adopted in the literature to estimate the RRL metallicity distribution in ω Cen (BR16) and in nearby dwarf galaxies (Martínez-Vázquez et al. 2016). The inversion of the PLZ relations is straightforward and relies on the following equation:

$$[\text{Fe}/\text{H}] = \frac{M_X - b_X \log P - a_X}{c_X}, \quad (1)$$

where *X* is for the photometric band (*I*, *J*, *H*, *K*) while the constants a_X , b_X , and c_X are the zero-point, the slope and the metallicity coefficient of the predicted PLZ relations ($M_X = a_X + b_X \log P + c_X [\text{Fe}/\text{H}]$). The coefficients a_X , b_X , and c_X are given by Marconi et al. (2015) and by M. Marconi et al. (2018, in preparation).

Figure 2 shows, moving counterclockwise, the metallicity distributions based on inversion of the *I*, *J*, *H*, *K* PLZ relations. The red and the blue lines display the metallicity distribution for RRab and RRc variables, while the black one shows the distribution for the global sample. In the global sample the periods of RRc variables were fundamentalized, i.e., $\log P_F = \log P_{FO} + 0.127$ (Coppola et al. 2015). The metallicity distributions were smoothed using a Gaussian kernel with the unit weight and σ equal to the uncertainty on the metallicity. The median of the three different metallicity distributions, together with their standard deviations, are labeled.

Data plotted in this figure show several interesting features.

(i) The standard deviations of the metallicity distributions based on NIR PLZ relations are systematically smaller than those based on the *I*-band PLZ relation. The difference is mainly caused by the increase in the slope and by the decrease in the intrinsic dispersion of the PLZ relations when moving from shorter to longer wavelengths. Marginal variations in the mean cluster reddening might also contribute to explaining the minimal difference among optical (*I*) and NIR (*J*, *H*, *K*) estimates.

(ii) The metallicity distributions for RRc and RRab agree quite well with each other at fixed photometric bands, thus suggesting similar metallicity distributions.

(iii) The metallicity distributions show several secondary bumps, suggestive of a multimodal distribution. However, the position and the fraction of stars included in these secondary features changes among the different bands. In spite of these variations there is evidence of a shoulder in the more metal-rich regime for $[\text{Fe}/\text{H}] \geq -1.5$. A closer inspection into the metallicity distribution, based on different assumptions concerning the smoothing, indicates that the current estimates display a well defined secondary peak for $[\text{Fe}/\text{H}] \sim -1.5$. This finding further supports the evidence that the RRL metallicity distribution in ω Cen is at least bimodal. In passing we also note that the metal-poor tail ($[\text{Fe}/\text{H}] \leq -2.5$) vanishes when moving from the *I* band to the *J*, *H*, *K* bands. This suggests that it might be affected by small reddening variations and/or uncertainties in the mean magnitudes.

(c)—the individual metallicities were estimated as the mean of the values based on the global relations in the three NIR (*J*, *H*, *K*)

²⁴ Note that throughout the paper we are using *K* instead of the 2MASS *K_s* band.

Table 1
Individual Iron Abundances, Reddenings, and True Distance Moduli for ω Cen RRLs Based on REDIME

ID ^a	Mode ^b	R.A. ^c	Decl. ^c	NM ^d	[Fe/H] ^e dex	RRc ^f $E(B - V)$ ^g mag	μ^h mag	[Fe/H] ^e dex	RRab ^f $E(B - V)$ ^g mag	μ^h mag	[Fe/H] ^e dex	Global ^f $E(B - V)$ ^g mag	μ^h mag
V3	0	201.483917	-47.431750	6	-1.79 ± 0.13	0.10 ± 0.01	13.74 ± 0.03	-1.79 ± 0.11	0.10 ± 0.01	13.74 ± 0.02
V4	0	201.553833	-47.405389	6	-2.16 ± 0.09	0.13 ± 0.01	13.71 ± 0.02	-2.12 ± 0.05	0.13 ± 0.01	13.71 ± 0.02
V5	0	201.576333	-47.386944	6	-1.33 ± 0.18	0.16 ± 0.01	13.70 ± 0.04	-1.26 ± 0.14	0.15 ± 0.01	13.71 ± 0.03
V7	0	201.754250	-47.233389	6	-2.01 ± 0.11	0.14 ± 0.01	13.71 ± 0.02	-1.99 ± 0.07	0.14 ± 0.01	13.72 ± 0.02
V8	0	201.951792	-47.472444	6	-1.90 ± 0.11	0.16 ± 0.01	13.70 ± 0.02	-1.84 ± 0.05	0.16 ± 0.01	13.71 ± 0.01
V9	0	201.498208	-47.440139	6	-1.46 ± 0.13	0.18 ± 0.01	13.70 ± 0.03	-1.40 ± 0.08	0.17 ± 0.01	13.71 ± 0.02
V10	1	201.529125	-47.410306	6	-1.79 ± 0.21	0.11 ± 0.01	13.70 ± 0.03	-2.11 ± 0.12	0.12 ± 0.01	13.72 ± 0.03
V11	0	201.627250	-47.383889	6	-1.98 ± 0.18	0.13 ± 0.01	13.69 ± 0.04	-2.08 ± 0.05	0.12 ± 0.01	13.72 ± 0.02
V12	1	201.613208	-47.401861	6	-2.16 ± 0.30	0.12 ± 0.01	13.76 ± 0.04	-2.05 ± 0.07	0.13 ± 0.01	13.71 ± 0.02
V13	0	201.492375	-47.422806	6	-2.13 ± 0.12	0.13 ± 0.01	13.71 ± 0.03	-2.16 ± 0.07	0.13 ± 0.01	13.73 ± 0.02
V14	1	201.498583	-47.652778	6	-1.33 ± 0.41	0.09 ± 0.02	13.69 ± 0.06	-1.91 ± 0.14	0.11 ± 0.01	13.73 ± 0.03
V15	0	201.612833	-47.410694	6	-1.86 ± 0.28	0.12 ± 0.01	13.68 ± 0.05	-2.10 ± 0.11	0.12 ± 0.01	13.72 ± 0.02
V16	1	201.907125	-47.626444	6	-2.01 ± 0.17	0.13 ± 0.01	13.72 ± 0.03	-1.90 ± 0.14	0.13 ± 0.01	13.72 ± 0.03
V18	0	201.937750	-47.415833	6	-2.19 ± 0.24	0.13 ± 0.01	13.76 ± 0.04	-1.94 ± 0.07	0.12 ± 0.01	13.73 ± 0.02
V19	1	201.875500	-47.468278	6	-1.90 ± 0.44	0.18 ± 0.01	13.76 ± 0.06	-1.40 ± 0.09	0.17 ± 0.01	13.71 ± 0.02
V20	0	201.808500	-47.468583	6	-1.73 ± 0.36	0.15 ± 0.01	13.64 ± 0.07	-2.05 ± 0.10	0.15 ± 0.01	13.71 ± 0.02
V21	1	201.546458	-47.433167	6	-1.46 ± 0.26	0.05 ± 0.01	13.75 ± 0.04	-1.82 ± 0.24	0.06 ± 0.01	13.76 ± 0.04
V22	1	201.921042	-47.568917	6	-1.98 ± 0.29	0.11 ± 0.01	13.77 ± 0.04	-1.94 ± 0.11	0.12 ± 0.01	13.73 ± 0.02
V23	0	201.693667	-47.411028	6	-2.10 ± 0.73	0.20 ± 0.02	13.81 ± 0.12	-1.31 ± 0.10	0.17 ± 0.01	13.70 ± 0.02
V24	1	201.909708	-47.570833	6	-2.13 ± 0.55	0.09 ± 0.02	13.83 ± 0.07	-2.04 ± 0.11	0.11 ± 0.01	13.74 ± 0.02
V25	0	201.606250	-47.473278	6	-1.92 ± 0.13	0.12 ± 0.01	13.70 ± 0.03	-1.99 ± 0.02	0.12 ± 0.01	13.73 ± 0.01
V26	0	201.598375	-47.449972	6	-1.98 ± 0.06	0.14 ± 0.01	13.71 ± 0.02	-1.98 ± 0.04	0.14 ± 0.01	13.72 ± 0.01
V27	0	201.608417	-47.471417	6	-1.46 ± 0.10	0.18 ± 0.01	13.66 ± 0.02	-1.50 ± 0.09	0.18 ± 0.01	13.68 ± 0.02
V30	1	201.566333	-47.499056	6	-1.86 ± 0.14	0.09 ± 0.01	13.76 ± 0.02	-2.00 ± 0.06	0.10 ± 0.01	13.73 ± 0.02
V32	0	201.763917	-47.360917	6	-2.08 ± 0.22	0.12 ± 0.01	13.76 ± 0.04	-1.83 ± 0.07	0.11 ± 0.01	13.74 ± 0.02
V33	0	201.464833	-47.485056	6	-1.62 ± 0.53	0.13 ± 0.01	13.63 ± 0.09	-2.08 ± 0.11	0.14 ± 0.01	13.73 ± 0.02
V34	0	201.529917	-47.553056	6	-1.70 ± 0.41	0.13 ± 0.01	13.65 ± 0.07	-2.08 ± 0.05	0.13 ± 0.01	13.72 ± 0.01
V35	1	201.721833	-47.376389	6	-2.19 ± 0.30	0.12 ± 0.01	13.77 ± 0.04	-2.09 ± 0.13	0.13 ± 0.01	13.72 ± 0.03
V36	1	201.792458	-47.258222	6	-1.73 ± 0.27	0.10 ± 0.01	13.70 ± 0.04	-2.13 ± 0.13	0.12 ± 0.01	13.73 ± 0.03
V38	0	201.763500	-47.608472	6	-1.38 ± 0.66	0.12 ± 0.01	13.61 ± 0.10	-2.02 ± 0.05	0.13 ± 0.01	13.72 ± 0.01
V39	1	201.999250	-47.578444	6	-2.10 ± 0.58	0.10 ± 0.02	13.82 ± 0.08	-1.79 ± 0.10	0.10 ± 0.01	13.74 ± 0.02
V40	0	201.602292	-47.513000	6	-1.59 ± 0.39	0.13 ± 0.01	13.65 ± 0.07	-1.94 ± 0.02	0.13 ± 0.01	13.72 ± 0.02
V41	0	201.755750	-47.517278	6	-2.03 ± 0.06	0.14 ± 0.01	13.71 ± 0.02	-1.96 ± 0.01	0.13 ± 0.01	13.71 ± 0.01
V44	0	201.593250	-47.576611	6	-1.99 ± 0.57	0.18 ± 0.01	13.79 ± 0.10	-1.37 ± 0.06	0.16 ± 0.01	13.70 ± 0.02
V45	0	201.378542	-47.455833	6	-1.54 ± 0.58	0.13 ± 0.01	13.62 ± 0.10	-2.06 ± 0.11	0.14 ± 0.01	13.72 ± 0.02
V46	0	201.375958	-47.431028	6	-1.75 ± 0.29	0.14 ± 0.01	13.69 ± 0.05	-2.00 ± 0.06	0.14 ± 0.01	13.74 ± 0.02
V47	1	201.485292	-47.403444	6	-1.92 ± 0.32	0.05 ± 0.01	13.82 ± 0.04	-2.13 ± 0.17	0.08 ± 0.01	13.76 ± 0.03
V49	0	201.532167	-47.632222	6	-1.87 ± 0.05	0.17 ± 0.01	13.70 ± 0.02	-1.80 ± 0.02	0.16 ± 0.01	13.70 ± 0.01
V50	1	201.474667	-47.460056	6	-1.98 ± 0.45	0.14 ± 0.01	13.77 ± 0.06	-1.77 ± 0.10	0.14 ± 0.01	13.70 ± 0.02
V51	0	201.677417	-47.406028	6	-2.12 ± 0.07	0.14 ± 0.01	13.71 ± 0.02	-2.12 ± 0.05	0.14 ± 0.01	13.72 ± 0.02
V52	0	201.646458	-47.467917	6	-2.10 ± 0.26	0.07 ± 0.01	13.71 ± 0.05	-2.28 ± 0.13	0.07 ± 0.01	13.76 ± 0.03
V54	0	201.597917	-47.313389	6	-1.91 ± 0.15	0.12 ± 0.01	13.69 ± 0.03	-2.04 ± 0.02	0.12 ± 0.01	13.72 ± 0.01
V56	0	201.481000	-47.629028	6	-1.99 ± 0.74	0.18 ± 0.02	13.83 ± 0.13	-1.20 ± 0.10	0.16 ± 0.01	13.71 ± 0.02
V57	0	201.955917	-47.614083	6	-2.04 ± 0.08	0.14 ± 0.01	13.70 ± 0.02	-2.01 ± 0.07	0.14 ± 0.01	13.70 ± 0.02
V58	1	201.554292	-47.400972	6	-1.46 ± 0.15	0.06 ± 0.01	13.75 ± 0.03	-1.75 ± 0.18	0.08 ± 0.01	13.75 ± 0.03
V59	0	201.576708	-47.496500	6	-1.53 ± 0.17	0.16 ± 0.01	13.68 ± 0.04	-1.52 ± 0.12	0.15 ± 0.01	13.70 ± 0.03

Table 1
(Continued)

ID ^a	Mode ^b	R.A. ^c	Decl. ^c	NM ^d	[Fe/H] ^e dex	RRc ^f $E(B - V)^g$ mag	μ^h mag	[Fe/H] ^e dex	RRab ^f $E(B - V)^g$ mag	μ^h mag	[Fe/H] ^e dex	Global ^f $E(B - V)^g$ mag	μ^h mag
V62	0	201.610708	-47.465556	6	-1.97 ± 0.17	0.11 ± 0.01	13.69 ± 0.03	-2.10 ± 0.04	0.11 ± 0.01	13.73 ± 0.02
V63	0	201.282792	-47.614972	6	-1.99 ± 0.09	0.13 ± 0.01	13.73 ± 0.02	-1.93 ± 0.05	0.13 ± 0.01	13.73 ± 0.02
V64	1	201.509000	-47.605472	6	-2.08 ± 0.14	0.13 ± 0.01	13.73 ± 0.02	-2.02 ± 0.13	0.13 ± 0.01	13.72 ± 0.03
V66	1	201.637583	-47.373806	6	-1.62 ± 0.26	0.10 ± 0.01	13.70 ± 0.04	-2.11 ± 0.11	0.13 ± 0.01	13.72 ± 0.03
V67	0	201.619000	-47.313139	6	-1.42 ± 0.10	0.15 ± 0.01	13.71 ± 0.02	-1.43 ± 0.06	0.14 ± 0.01	13.72 ± 0.02
V69	0	201.295542	-47.625917	6	-2.11 ± 0.27	0.13 ± 0.03	13.76 ± 0.05	-1.82 ± 0.07	0.12 ± 0.03	13.72 ± 0.03
V70	1	201.865625	-47.562028	6	-1.70 ± 0.24	0.10 ± 0.01	13.71 ± 0.04	-2.12 ± 0.10	0.11 ± 0.01	13.73 ± 0.02
V71	1	201.783583	-47.464528	6	-1.38 ± 0.42	0.10 ± 0.01	13.66 ± 0.06	-1.90 ± 0.09	0.12 ± 0.01	13.72 ± 0.02
V72	1	201.887583	-47.273000	6	-1.59 ± 0.27	0.09 ± 0.01	13.71 ± 0.04	-2.00 ± 0.15	0.11 ± 0.01	13.74 ± 0.03
V73	0	201.473542	-47.269639	6	-2.02 ± 0.15	0.21 ± 0.04	13.70 ± 0.04	-1.87 ± 0.06	0.20 ± 0.04	13.69 ± 0.03
V74	0	201.780208	-47.292889	6	-1.62 ± 0.28	0.14 ± 0.01	13.66 ± 0.05	-1.81 ± 0.08	0.13 ± 0.01	13.71 ± 0.02
V75	1	201.832042	-47.313083	6	-2.03 ± 0.11	0.12 ± 0.01	13.72 ± 0.02	-2.31 ± 0.12	0.14 ± 0.01	13.71 ± 0.03
V76	1	201.738667	-47.335556	6	-1.99 ± 0.26	0.11 ± 0.01	13.73 ± 0.04	-1.98 ± 0.26	0.11 ± 0.01	13.74 ± 0.04
V77	1	201.836958	-47.368389	6	-1.54 ± 0.28	0.10 ± 0.01	13.69 ± 0.04	-2.12 ± 0.10	0.13 ± 0.01	13.71 ± 0.03
V79	0	202.104458	-47.490250	6	-1.85 ± 0.08	0.14 ± 0.01	13.69 ± 0.02	-1.80 ± 0.04	0.14 ± 0.01	13.70 ± 0.01
V81	1	201.902667	-47.413583	6	-1.75 ± 0.10	0.11 ± 0.01	13.72 ± 0.02	-2.02 ± 0.10	0.13 ± 0.01	13.73 ± 0.02
V82	1	201.898250	-47.441917	6	-1.87 ± 0.56	0.13 ± 0.02	13.64 ± 0.08	-2.34 ± 0.16	0.14 ± 0.01	13.72 ± 0.03
V83	1	201.785125	-47.359611	6	-2.12 ± 0.19	0.12 ± 0.01	13.74 ± 0.03	-2.03 ± 0.13	0.12 ± 0.01	13.72 ± 0.03
V85	0	201.277458	-47.392694	6	-1.54 ± 0.29	0.12 ± 0.01	13.67 ± 0.05	-1.81 ± 0.04	0.12 ± 0.01	13.72 ± 0.01
V86	0	201.813208	-47.436583	6	-2.16 ± 0.08	0.15 ± 0.01	13.70 ± 0.02	-2.06 ± 0.05	0.15 ± 0.01	13.70 ± 0.02
V87	1	201.739458	-47.426611	6	-2.10 ± 0.26	0.13 ± 0.01	13.75 ± 0.04	-2.06 ± 0.05	0.14 ± 0.01	13.71 ± 0.02
V88	0	201.732917	-47.421306	6	-2.31 ± 0.62	0.13 ± 0.02	13.83 ± 0.11	-1.68 ± 0.08	0.11 ± 0.01	13.73 ± 0.02
V89	1	201.691500	-47.433694	6	-1.91 ± 0.15	0.16 ± 0.01	13.69 ± 0.03	-2.14 ± 0.03	0.17 ± 0.01	13.70 ± 0.02
V90	0	201.690500	-47.439917	6	-2.06 ± 0.16	0.13 ± 0.01	13.73 ± 0.03	-2.04 ± 0.13	0.12 ± 0.01	13.75 ± 0.03
V91	0	201.710750	-47.437722	6	-1.25 ± 0.92	0.10 ± 0.02	13.57 ± 0.14	-2.17 ± 0.03	0.12 ± 0.01	13.72 ± 0.02
V94	1	201.487792	-47.379583	6	-1.99 ± 0.33	0.17 ± 0.01	13.72 ± 0.05	-1.40 ± 0.16	0.14 ± 0.01	13.71 ± 0.03
V95	1	201.353708	-47.481389	6	-2.04 ± 0.29	0.13 ± 0.01	13.75 ± 0.04	-2.03 ± 0.14	0.14 ± 0.01	13.71 ± 0.03
V96	0	201.663625	-47.450944	6	-2.02 ± 0.32	0.14 ± 0.01	13.65 ± 0.06	-2.30 ± 0.06	0.14 ± 0.01	13.71 ± 0.02
V97	0	201.785375	-47.425417	6	-1.53 ± 0.53	0.12 ± 0.01	13.63 ± 0.09	-2.04 ± 0.03	0.12 ± 0.01	13.73 ± 0.01
V98	1	201.774333	-47.449222	6	-1.53 ± 0.12	0.17 ± 0.01	13.68 ± 0.02	-1.39 ± 0.12	0.16 ± 0.01	13.70 ± 0.03
V99	0	201.758917	-47.463722	6	-1.58 ± 0.74	0.07 ± 0.02	13.63 ± 0.12	-2.30 ± 0.09	0.08 ± 0.01	13.75 ± 0.02
V100	0	201.766750	-47.459417	6	-2.13 ± 0.69	0.15 ± 0.02	13.80 ± 0.12	-1.39 ± 0.09	0.14 ± 0.01	13.70 ± 0.02
V101	1	201.875917	-47.497694	6	-1.97 ± 0.14	0.13 ± 0.01	13.73 ± 0.03	-1.94 ± 0.14	0.13 ± 0.01	13.72 ± 0.03
V102	0	201.842042	-47.503611	6	-1.93 ± 0.11	0.15 ± 0.01	13.69 ± 0.03	-2.02 ± 0.01	0.15 ± 0.01	13.71 ± 0.02
V103	1	201.809458	-47.476917	6	-1.99 ± 0.26	0.12 ± 0.01	13.68 ± 0.04	-2.16 ± 0.12	0.12 ± 0.01	13.72 ± 0.03
V104	0	202.032500	-47.562472	6	-2.00 ± 0.40	0.14 ± 0.01	13.78 ± 0.07	-1.60 ± 0.04	0.13 ± 0.01	13.72 ± 0.01
V105	1	201.941792	-47.545639	6	-1.42 ± 0.11	0.14 ± 0.01	13.71 ± 0.02	-1.48 ± 0.11	0.15 ± 0.01	13.71 ± 0.02
V106	0	201.746500	-47.470278	6	-1.86 ± 0.26	0.13 ± 0.01	13.68 ± 0.05	-2.05 ± 0.07	0.13 ± 0.01	13.73 ± 0.02
V107	0	201.808458	-47.516250	6	-1.48 ± 0.10	0.17 ± 0.01	13.68 ± 0.02	-1.51 ± 0.02	0.17 ± 0.01	13.70 ± 0.01
V108	0	201.769458	-47.490611	6	-1.85 ± 0.31	0.14 ± 0.01	13.66 ± 0.06	-2.12 ± 0.01	0.14 ± 0.01	13.72 ± 0.01
V109	0	201.756375	-47.493639	6	-1.93 ± 0.13	0.11 ± 0.01	13.71 ± 0.03	-2.03 ± 0.02	0.11 ± 0.01	13.74 ± 0.01
V110	1	201.758542	-47.502000	6	-2.11 ± 0.34	0.13 ± 0.01	13.76 ± 0.05	-1.79 ± 0.13	0.13 ± 0.01	13.73 ± 0.03
V111	0	201.704125	-47.477944	6	-1.80 ± 0.30	0.15 ± 0.01	13.65 ± 0.06	-2.03 ± 0.18	0.15 ± 0.01	13.70 ± 0.04
V112	0	201.726000	-47.506583	6	-1.82 ± 0.35	0.08 ± 0.01	13.79 ± 0.06	-1.42 ± 0.17	0.07 ± 0.01	13.75 ± 0.04
V113	0	201.734583	-47.530000	6	-1.92 ± 0.15	0.15 ± 0.01	13.73 ± 0.03	-1.75 ± 0.06	0.14 ± 0.01	13.72 ± 0.02
V114	0	201.708792	-47.505972	6	-1.87 ± 0.16	0.13 ± 0.01	13.71 ± 0.03	-1.85 ± 0.14	0.12 ± 0.01	13.72 ± 0.03

Table 1
(Continued)

ID ^a	Mode ^b	R.A. ^c	Decl. ^c	NM ^d	[Fe/H] ^e dex	RRc ^f	μ^h mag	[Fe/H] ^e dex	RRab ^f	μ^h mag	[Fe/H] ^e dex	Global ^f	μ^h mag
						$E(B - V)^g$ mag			$E(B - V)^g$ mag			$E(B - V)^g$ mag	
V115	0	201.551125	-47.571694	6	-2.04 ± 0.09	0.14 ± 0.01	13.71 ± 0.02	-2.00 ± 0.06	0.14 ± 0.01	13.71 ± 0.02
V116	0	201.647833	-47.468694	6	-1.98 ± 0.28	0.12 ± 0.01	13.74 ± 0.05	-1.74 ± 0.15	0.11 ± 0.01	13.71 ± 0.03
V117	1	201.582875	-47.489361	6	-2.02 ± 0.34	0.10 ± 0.01	13.79 ± 0.05	-2.01 ± 0.12	0.12 ± 0.01	13.73 ± 0.02
V118	0	201.668917	-47.505417	6	-1.81 ± 1.42	0.20 ± 0.03	13.41 ± 0.20	-3.19 ± 0.08	0.22 ± 0.01	13.66 ± 0.02
V119	1	201.659500	-47.521778	6	-1.62 ± 0.49	0.14 ± 0.01	13.64 ± 0.07	-1.96 ± 0.10	0.14 ± 0.01	13.71 ± 0.02
V120	0	201.606333	-47.547000	6	-1.84 ± 0.32	0.18 ± 0.01	13.73 ± 0.06	-1.48 ± 0.09	0.17 ± 0.01	13.69 ± 0.02
V121	1	201.617333	-47.530861	6	-1.85 ± 0.66	0.14 ± 0.02	13.61 ± 0.09	-2.28 ± 0.12	0.14 ± 0.01	13.71 ± 0.03
V122	0	201.626250	-47.550750	6	-1.82 ± 0.31	0.15 ± 0.01	13.65 ± 0.06	-2.08 ± 0.08	0.15 ± 0.01	13.71 ± 0.02
V123	1	201.712792	-47.620389	6	-1.54 ± 0.31	0.06 ± 0.01	13.82 ± 0.05	-1.78 ± 0.14	0.09 ± 0.01	13.75 ± 0.03
V124	1	201.726583	-47.652139	6	-2.16 ± 0.22	0.14 ± 0.01	13.75 ± 0.03	-1.95 ± 0.14	0.13 ± 0.01	13.74 ± 0.03
V125	0	201.704042	-47.684361	6	-2.41 ± 0.51	0.17 ± 0.01	13.79 ± 0.10	-1.87 ± 0.08	0.16 ± 0.01	13.71 ± 0.04
V126	1	202.033875	-47.679583	6	-2.31 ± 0.53	0.12 ± 0.02	13.79 ± 0.08	-1.83 ± 0.09	0.12 ± 0.01	13.73 ± 0.02
V127	1	201.330917	-47.477111	6	-2.06 ± 0.15	0.14 ± 0.01	13.71 ± 0.03	-1.89 ± 0.16	0.13 ± 0.01	13.72 ± 0.03
V128	0	201.573875	-47.503806	6	-1.96 ± 0.27	0.11 ± 0.02	13.69 ± 0.06	-2.22 ± 0.07	0.11 ± 0.02	13.73 ± 0.04
V130	0	201.541667	-47.227778	6	-1.83 ± 0.30	0.18 ± 0.01	13.74 ± 0.05	-1.46 ± 0.06	0.17 ± 0.01	13.70 ± 0.02
V131	1	201.625208	-47.494806	6	-1.25 ± 0.80	0.09 ± 0.02	13.62 ± 0.09	-2.22 ± 0.07	0.12 ± 0.01	13.72 ± 0.02
V132	0	201.663292	-47.486167	6	-2.10 ± 0.16	0.12 ± 0.01	13.68 ± 0.04	-2.21 ± 0.08	0.12 ± 0.01	13.72 ± 0.02
V134	0	201.305458	-47.207889	6	-1.84 ± 0.19	0.15 ± 0.01	13.66 ± 0.04	-1.89 ± 0.13	0.14 ± 0.01	13.69 ± 0.03
V135	0	201.616958	-47.488444	6	-1.71 ± 0.92	0.13 ± 0.02	13.55 ± 0.14	-2.54 ± 0.28	0.14 ± 0.01	13.70 ± 0.06
V136	1	201.629458	-47.461389	6	-2.02 ± 0.10	0.07 ± 0.01	13.74 ± 0.02	-2.23 ± 0.12	0.09 ± 0.01	13.74 ± 0.03
V137	1	201.631333	-47.451333	6	-1.53 ± 0.69	0.13 ± 0.02	13.62 ± 0.09	-2.17 ± 0.07	0.14 ± 0.01	13.71 ± 0.02
V139	0	201.657208	-47.459889	6	-2.02 ± 1.37	0.18 ± 0.03	13.43 ± 0.20	-3.37 ± 0.07	0.20 ± 0.01	13.67 ± 0.02
V140	0	201.675458	-47.502000	6	-2.08 ± 0.11	0.08 ± 0.01	13.75 ± 0.03	-2.02 ± 0.13	0.07 ± 0.01	13.76 ± 0.03
V141	0	201.670333	-47.491194	6	-2.16 ± 0.16	0.15 ± 0.01	13.68 ± 0.03	-2.30 ± 0.03	0.15 ± 0.01	13.71 ± 0.02
V143	0	201.677458	-47.458083	6	-1.71 ± 0.63	0.12 ± 0.03	13.60 ± 0.10	-2.32 ± 0.15	0.12 ± 0.02	13.71 ± 0.03
V144	0	201.679292	-47.471722	6	-1.77 ± 0.38	0.14 ± 0.01	13.65 ± 0.07	-2.13 ± 0.13	0.14 ± 0.01	13.71 ± 0.03
V145	1	201.713417	-47.519139	6	-1.58 ± 0.10	0.12 ± 0.01	13.70 ± 0.02	-1.85 ± 0.09	0.14 ± 0.01	13.71 ± 0.02
V146	0	201.720167	-47.491194	6	-2.33 ± 0.59	0.14 ± 0.02	13.79 ± 0.11	-1.74 ± 0.19	0.13 ± 0.01	13.71 ± 0.04
V147	1	201.816208	-47.519528	6	-2.13 ± 0.11	0.10 ± 0.01	13.74 ± 0.02	-2.35 ± 0.17	0.12 ± 0.01	13.72 ± 0.03
V149	0	201.886875	-47.228722	6	-2.06 ± 0.13	0.14 ± 0.01	13.72 ± 0.03	-1.98 ± 0.09	0.14 ± 0.01	13.72 ± 0.02
V150	0	201.917625	-47.600139	6	-1.55 ± 0.49	0.07 ± 0.01	13.66 ± 0.09	-2.00 ± 0.18	0.07 ± 0.01	13.73 ± 0.04
V153	1	201.706875	-47.440000	6	-1.93 ± 0.16	0.15 ± 0.01	13.72 ± 0.03	-1.99 ± 0.06	0.16 ± 0.01	13.69 ± 0.02
V154	1	201.763000	-47.509222	6	-2.00 ± 0.12	0.13 ± 0.01	13.70 ± 0.02	-1.96 ± 0.14	0.13 ± 0.01	13.71 ± 0.03
V155	1	201.723500	-47.411917	6	-1.86 ± 0.09	0.12 ± 0.01	13.73 ± 0.02	-2.06 ± 0.05	0.13 ± 0.01	13.71 ± 0.02
V156	1	201.699833	-47.531500	5	-1.48 ± 0.58	0.12 ± 0.02	13.63 ± 0.11	-2.12 ± 0.10	0.14 ± 0.01	13.72 ± 0.06
V157	1	201.693583	-47.454944	6	-1.85 ± 0.26	0.14 ± 0.01	13.73 ± 0.04	-2.03 ± 0.20	0.16 ± 0.01	13.71 ± 0.04
V158	1	201.688792	-47.511250	6	-1.93 ± 0.21	0.11 ± 0.01	13.75 ± 0.03	-1.88 ± 0.13	0.12 ± 0.01	13.72 ± 0.03
V160	1	201.400292	-47.208972	6	-1.80 ± 0.16	0.10 ± 0.01	13.75 ± 0.03	-1.91 ± 0.11	0.11 ± 0.01	13.72 ± 0.03
V163	1	201.456125	-47.339389	6	-1.82 ± 0.23	0.11 ± 0.01	13.71 ± 0.04	-1.88 ± 0.18	0.11 ± 0.01	13.74 ± 0.03
V165	0	201.664083	-47.448889	3	-2.31 ± 0.83	0.12 ± 0.09	13.87 ± 0.17	-1.43 ± 0.10	0.18 ± 0.06	13.69 ± 0.04
V169	1	201.835208	-47.399917	6	-1.92 ± 0.18	0.12 ± 0.01	13.74 ± 0.03	-1.72 ± 0.11	0.11 ± 0.01	13.73 ± 0.03
V184	1	201.868708	-47.526694	6	-1.87 ± 0.24	0.14 ± 0.01	13.68 ± 0.04	-1.93 ± 0.14	0.13 ± 0.01	13.73 ± 0.03
V185	1	201.516917	-47.363056	6	-2.04 ± 0.29	0.08 ± 0.01	13.78 ± 0.04	-1.80 ± 0.18	0.08 ± 0.01	13.75 ± 0.03
V261	1	201.814167	-47.358333	6	-1.98 ± 0.85	0.20 ± 0.02	13.55 ± 0.11	-2.91 ± 0.03	0.22 ± 0.01	13.66 ± 0.02
V263	0	201.554625	-47.436194	6	-1.45 ± 0.50	0.08 ± 0.01	13.67 ± 0.08	-1.95 ± 0.08	0.09 ± 0.01	13.75 ± 0.02
V264	1	201.665167	-47.507944	6	-1.81 ± 0.43	0.15 ± 0.01	13.76 ± 0.06	-1.42 ± 0.04	0.14 ± 0.01	13.71 ± 0.02

Table 1
(Continued)

ID ^a	Mode ^b	R.A. ^c	Decl. ^c	NM ^d	[Fe/H] ^e dex	RRc ^f $E(B - V)$ ^g mag	μ ^h mag	[Fe/H] ^e dex	RRab ^f $E(B - V)$ ^g mag	μ ^h mag	[Fe/H] ^e dex	Global ^f $E(B - V)$ ^g mag	μ ^h mag
V265	1	201.625833	-47.479361	6	-1.84 ± 0.13	0.11 ± 0.01	13.71 ± 0.02	-2.24 ± 0.05	0.13 ± 0.01	13.71 ± 0.02
V266	1	201.665042	-47.467250	6	-1.82 ± 0.13	0.11 ± 0.01	13.71 ± 0.02	-1.96 ± 0.13	0.12 ± 0.01	13.72 ± 0.03
V267	1	201.667458	-47.443361	6	-2.41 ± 0.20	0.12 ± 0.01	13.73 ± 0.04	-2.11 ± 0.10	0.11 ± 0.01	13.72 ± 0.03
V268	0	201.646292	-47.436472	5	-1.91 ± 0.17	0.15 ± 0.01	13.68 ± 0.10	-2.07 ± 0.02	0.15 ± 0.01	13.71 ± 0.09
V270	1	201.735542	-47.501722	6	-1.96 ± 0.18	0.12 ± 0.01	13.69 ± 0.03	-1.99 ± 0.14	0.11 ± 0.01	13.72 ± 0.03
V271	1	201.696250	-47.501194	6	-1.83 ± 0.14	0.12 ± 0.02	13.74 ± 0.03	-2.10 ± 0.14	0.15 ± 0.02	13.71 ± 0.03
V272	1	201.678792	-47.432472	6	-2.10 ± 0.19	0.15 ± 0.01	13.68 ± 0.03	-2.10 ± 0.14	0.15 ± 0.01	13.71 ± 0.03
V273	1	201.726375	-47.452528	6	-1.84 ± 0.05	0.13 ± 0.01	13.71 ± 0.02	-2.00 ± 0.08	0.14 ± 0.01	13.71 ± 0.02
V274	1	201.682167	-47.380111	6	-1.71 ± 0.32	0.12 ± 0.01	13.68 ± 0.05	-1.89 ± 0.16	0.12 ± 0.01	13.73 ± 0.03
V275	1	201.707208	-47.460417	6	-2.02 ± 0.10	0.13 ± 0.01	13.72 ± 0.02	-2.08 ± 0.10	0.14 ± 0.01	13.70 ± 0.03
V276	1	201.818708	-47.555056	6	-2.08 ± 0.19	0.14 ± 0.01	13.69 ± 0.03	-2.07 ± 0.14	0.13 ± 0.01	13.72 ± 0.03
V277	1	201.749792	-47.458250	6	-2.16 ± 0.19	0.11 ± 0.01	13.74 ± 0.03	-2.08 ± 0.16	0.11 ± 0.01	13.73 ± 0.03
V280	1	201.788875	-47.385083	6	-1.71 ± 0.19	0.13 ± 0.01	13.73 ± 0.03	-1.41 ± 0.12	0.11 ± 0.01	13.73 ± 0.02
V285	1	201.417083	-47.580167	6	-1.77 ± 0.15	0.11 ± 0.01	13.73 ± 0.03	-1.76 ± 0.17	0.11 ± 0.01	13.74 ± 0.03
V288	1	202.043333	-47.396556	6	-2.33 ± 0.37	0.14 ± 0.01	13.75 ± 0.06	-1.84 ± 0.17	0.12 ± 0.01	13.72 ± 0.03
V289	1	202.014792	-47.357778	6	-2.06 ± 0.14	0.15 ± 0.01	13.70 ± 0.02	-1.93 ± 0.15	0.14 ± 0.01	13.71 ± 0.03
V291	1	201.660500	-47.557889	6	-1.55 ± 0.61	0.08 ± 0.02	13.66 ± 0.08	-2.11 ± 0.17	0.10 ± 0.01	13.75 ± 0.03
NV339	1	201.623583	-47.497889	6	-2.31 ± 0.47	0.14 ± 0.02	13.63 ± 0.07	-2.49 ± 0.18	0.14 ± 0.01	13.70 ± 0.04
NV340	1	201.662125	-47.459167	6	-1.45 ± 0.82	0.12 ± 0.02	13.59 ± 0.10	-2.08 ± 0.11	0.13 ± 0.01	13.72 ± 0.02
NV341	1	201.727625	-47.480139	6	-1.91 ± 0.49	0.13 ± 0.02	13.63 ± 0.07	-2.21 ± 0.11	0.13 ± 0.01	13.71 ± 0.03
NV343	1	201.699125	-47.493778	6	-2.04 ± 0.29	0.14 ± 0.01	13.66 ± 0.04	-2.12 ± 0.19	0.13 ± 0.01	13.70 ± 0.04
NV344	1	201.658458	-47.412500	6	-2.23 ± 0.28	0.12 ± 0.01	13.75 ± 0.05	-1.90 ± 0.17	0.11 ± 0.01	13.73 ± 0.04
NV346	1	201.695500	-47.470667	6	-1.60 ± 0.67	0.11 ± 0.02	13.61 ± 0.09	-2.18 ± 0.12	0.12 ± 0.01	13.71 ± 0.03
NV347	1	201.574500	-47.483194	6	-1.40 ± 1.40	0.14 ± 0.03	13.48 ± 0.15	-2.63 ± 0.19	0.16 ± 0.01	13.67 ± 0.04
NV349	1	201.715792	-47.462306	6	-2.10 ± 0.57	0.12 ± 0.02	13.64 ± 0.09	-2.64 ± 0.17	0.13 ± 0.02	13.71 ± 0.05
NV350	1	201.734875	-47.514083	6	-1.57 ± 0.42	0.11 ± 0.01	13.66 ± 0.06	-2.13 ± 0.12	0.13 ± 0.01	13.71 ± 0.03
NV352	1	201.726583	-47.486722	6	-2.16 ± 0.62	0.13 ± 0.02	13.64 ± 0.09	-2.81 ± 0.19	0.15 ± 0.01	13.71 ± 0.04
NV353	1	201.682417	-47.465806	6	-2.05 ± 0.61	0.14 ± 0.02	13.62 ± 0.09	-2.70 ± 0.23	0.17 ± 0.01	13.68 ± 0.05
NV354	1	201.660750	-47.419528	6	-1.78 ± 0.10	0.11 ± 0.01	13.72 ± 0.02	-2.13 ± 0.09	0.14 ± 0.01	13.71 ± 0.02
NV357	1	201.573958	-47.506694	6	-2.04 ± 0.24	0.14 ± 0.01	13.67 ± 0.04	-2.07 ± 0.11	0.14 ± 0.01	13.72 ± 0.03
NV366	0	201.673125	-47.528444	6	-2.04 ± 0.94	0.07 ± 0.02	13.59 ± 0.15	-2.99 ± 0.17	0.09 ± 0.01	13.74 ± 0.03
NV399	1	201.623000	-47.500889	6	-1.49 ± 0.42	0.12 ± 0.01	13.67 ± 0.06	-1.81 ± 0.13	0.12 ± 0.01	13.73 ± 0.03

Notes.^a Variable identification according to Braga et al. (2016).^b Pulsation mode: 0—RRab; 1—RRc.^c R.A. and Decl. according to Braga et al. (2016).^d Number of mean magnitudes adopted for the REDIME solution.^e Mean iron abundance and standard deviation based on NIR (J, H, K) PL relations.^f Parameter estimates based on RRc, RRab, and global REDIME solution.^g Reddening and its uncertainty.^h True distance modulus and its uncertainty.

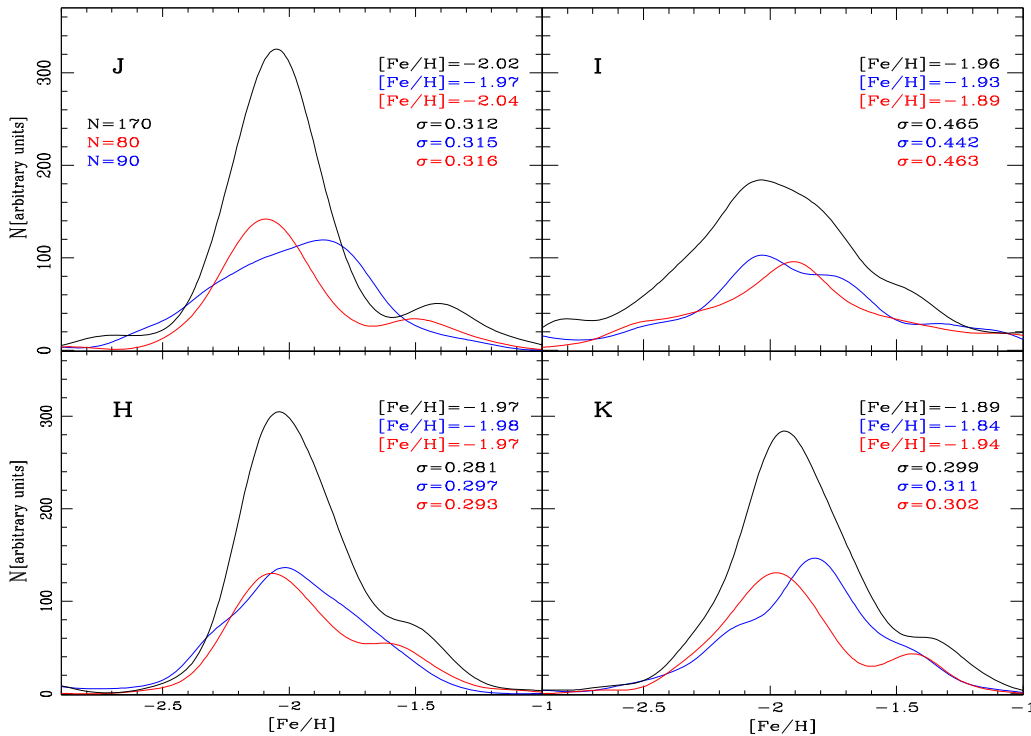


Figure 2. Metallicity distribution of RRLs in ω Cen using optical (I) and NIR (J, H, K) period–luminosity relations. To estimate the metal abundances we adopted a fixed true distance modulus ($\mu = 13.698$ mag, BR18) and a mean cluster reddening ($E(B - V) = 0.11$ mag Calamida et al. 2005). The metallicity distributions were smoothed using a Gaussian kernel with unit weight and σ equal to the error of the individual estimates. The red and the blue lines display the metallicity distribution for RRab and RRc variables, while the black line shows the metallicity distribution of the global sample. The median values and the standard deviation of the metallicity distributions are also labeled.

bands. The uncertainty was assumed to be equal to the mean standard deviation and it is typically smaller than 0.3 dex. Note that in estimating the error on the metallicity estimates we neglected the standard deviations of the predicted PLZ relations, since they are of the order of a few hundredths of a magnitude in the NIR bands (see Table 6 in Marconi et al. 2015). On the basis of the new individual mean metal abundances, we applied the same approach adopted by Inno et al. (2016) to estimate simultaneously the reddening and the true distance modulus. In particular, we seek to optimize the value of

$$\chi^2 = \sum_{j=1}^6 \left(\frac{\mu_j - (\mu + \xi_j E(B - V))}{\sigma_j} \right)^2, \quad (2)$$

where the sum runs over the four PLZ relations (I, J, H, K) and the two MZ relations (B, V), μ_j are the apparent distance moduli, $m_j - M_j$, in which the absolute magnitudes are based on pulsation predictions by Marconi et al. (2015), μ is the true distance modulus, ξ_j are the extinction coefficients according to the reddening law provided by Cardelli et al. (1989) with a constant total-to-selective absorption ratio ($R_V = 3.1$), and σ_j are the standard deviations taking into account uncertainties on apparent mean magnitudes, on absolute magnitudes (standard deviations of both PLZ and MZ relations), and on the extinction coefficients (Inno et al. 2016). The two free parameters are μ and $E(B - V)$.

Figure 3 shows the individual nonlinear fits over the the six optical/NIR measurements in the true distance modulus versus the inverse of the central wavelength. This means that for each variable in our sample we performed in this plane a nonlinear

fit (black line), based on the reddening law by Cardelli et al. (1989), over its six optical/NIR mean RRL magnitudes. Data plotted in this figure show that the true distance modulus ($\lambda \rightarrow \infty$) is mainly constrained by longer wavelength J-, H-, and in particular, K-band mean magnitudes. The slope of the nonlinear fit, and in turn, the reddening, are mainly constrained by shorter wavelength B-, V-, and I-band mean magnitudes. This “star-by-star” multi-wavelength, reddening, and true distance modulus plot was first introduced by Rich et al. (2014) in their parallel study of Cepheids in NGC 6822 (see their Figures 5 and 6). The difference in the dispersion when moving from optical to NIR measurements is due to intrinsic and extrinsic effects.

Intrinsic. The dispersion in magnitude, at fixed stellar parameters (stellar mass, luminosity, chemical composition), decreases when moving from the optical to the NIR bands. This is because NIR bands are less prone to uncertainties caused by evolutionary effects (off-ZAHB evolution).

Extrinsic Optical light curves are more prone to uncertainties caused by a non-optimal coverage of the light curve, because the luminosity amplitude steadily increases when moving from the K to the B band. Moreover, differential changes in the mean cluster reddening manifest themselves to a larger degree at shorter wavelengths.

The left panel of Figure 4 shows the true distance modulus distribution for the three different samples: RRc, RRab, and global. The distance distributions agree quite well with each other, and indeed, the difference in the median value is of the order of 1%. They are also quite symmetric and the standard deviations also attain similar values. On the other hand, the reddening distributions plotted on the right panel of the same

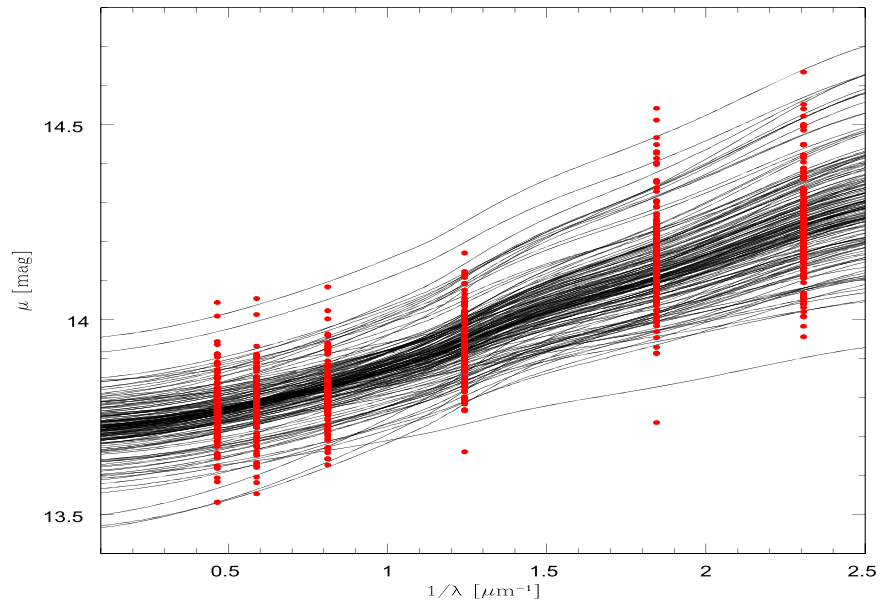


Figure 3. True distance modulus vs. the inverse of the central wavelength of the adopted photometric bands. The solid lines display the individual nonlinear fits to the six different apparent distance moduli. From right to left the red dots display the apparent moduli based on optical (B , V , I) and on NIR (J , H , K) mean magnitudes.

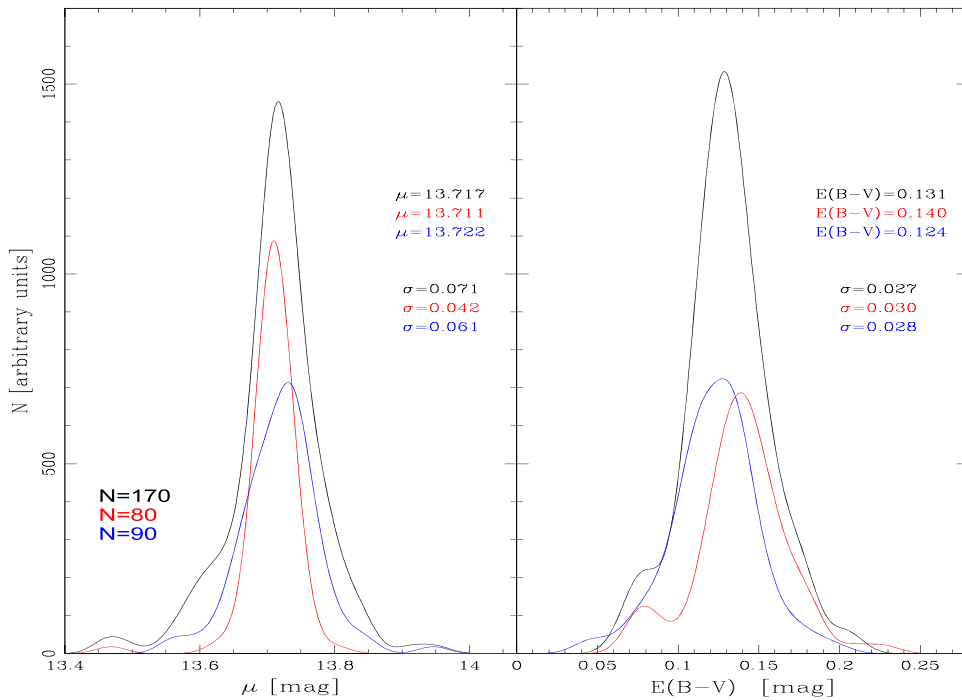


Figure 4. Left: true distance modulus distribution of ω Cen RR Lyrae stars. The individual distances were estimated using two mean magnitude–metallicity relations (M_B, M_V) and four period–luminosity–metallicity relations (I, J, H, K). The nonlinear fit was performed using the analytical reddening law provided by Cardelli et al. (1989) and extinction coefficients provided by Stetson et al. (2014). The individual metallicity evaluations adopted to estimate the distances are discussed in Section 3. The red and the blue lines display the distance distribution for R Rab and R Rc, while the black line is the global solution. The number of RRLs adopted for the three different solutions is labeled in the bottom left corner together with the median and the standard deviations. The distance distributions were smoothed using the same approach adopted to smooth the metallicity distributions. Right: same as the left, but for the reddening. The individual reddening estimates were simultaneously estimated with the true distance modulus performing the nonlinear fit with the Cardelli’s reddening law. The median and the standard deviations of the reddening distributions are also labeled.

figure suggest that the R Rab variables (red line) seem to have reddenings larger than R Rc (blue line) variables. However, the difference is of the order of 0.5σ . As expected, the color excess of the global sample attains reddening values that are intermediate between R Rab and R Rc variables.

The mean iron abundance, the true distance modulus, and the reddening after the first iteration for the three different samples

are listed in columns 2, 3, and 4 of Table 2 together with their means.

Second iteration: (d)—on the basis of the new median reddening and true distance modulus (global sample) we provided a new estimate of the individual metal abundances by inverting once again the I, J, H, K PLZ relations. The median and the σ of the new metallicity distributions agree quite well

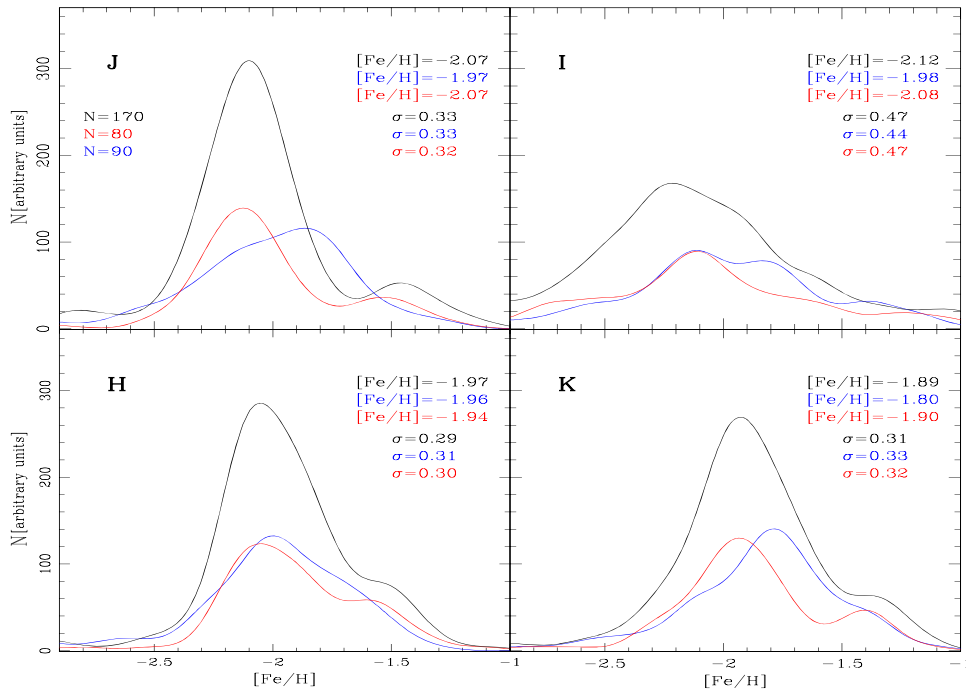


Figure 5. Same as Figure 2, but the metallicity estimates are based on individual reddening determinations and true distance moduli of RRLs obtained in the first iteration of REDIME.

with the metallicity distributions we obtained in the first iteration of REDIME. The agreement applies not only to the global sample, but also to the RRc and to the RRab sample. Indeed, the difference is on average smaller than 0.1 dex, thus suggesting that the solutions are quite stable.

The metallicity distributions plotted in Figure 5 indicate that metallicity estimates based on NIR diagnostics have standard deviations that are 0.1 dex smaller when compared with the *I* band. Moreover, they are also quite homogeneous, and indeed the difference in standard deviations is at most a few hundredths of a dex. This is the reason why we performed a mean of the NIR bands and we found $\langle [\text{Fe}/\text{H}] \rangle = -1.98 \pm 0.05$ and a standard deviation $\sigma = 0.54$ dex. The first error is the error on the mean and it is quite small due to the sample size. The second error is the standard deviation of the metallicity distribution and it is mainly caused by the intrinsic spread in metal abundance of stellar populations in ω Cen (Hughes & Wallerstein 2000; Johnson & Pilachowski 2010). The solutions for the three different samples (RRc, RRab, global) are given in column 5 of Table 2.

(e)—the new individual mean metal abundances were used to perform new nonlinear fits (Equation (2)) of the six mean magnitudes. The individual fits plotted in Figure 6 display the significant improvement in the distance modulus and reddening solution when moving from the first to the second iteration. The difference in lower and upper envelope in true distance moduli decreases from roughly ~ 0.5 to less than 0.1 mag in the NIR regime and from ~ 0.8 to ~ 0.6 mag in the optical regime. This evidence further supports the improvement on the individual mean metallicities. Note that the metallicity estimates are only based on the inversion of *J*-, *H*-, *K*-band PLZ relations, while the simultaneous solution for distance and reddening also relies on two MZ relations (*B*, *V*) and on the *I*-band PLZ relation.

(f)—the improvement between the first and the second iteration of REDIME becomes even more clear comparing the distribution of the true distance moduli plotted in the left panel

of Figure 4 and of Figure 7. The median cluster true distance moduli among the three different samples agree at the level of 1%. The σ of the global sample is a factor of two smaller when compared with the distribution obtained at the first iteration.

The new reddening distributions plotted in the right panel of Figure 7 agree quite well with those based on the first iteration, further supporting the stability of the solution. We also performed a third iteration, but the results are, within the errors, identical to the second one.

4. Internal Consistency

To further constrain the internal consistency of REDIME, Figure 8 displays the distribution of the current sample of RRLs in the absolute mean magnitude–metallicity plane. The RRLs display, as expected, a steady increase in the absolute mean magnitude as a function of the metal content. Data plotted in this figure also show that the spread in visual magnitudes is, at fixed metal content, systematically larger than that in the *B* band.

There is also evidence that RRc (empty symbols) variables in the *V* band and for metal abundances ranging from $[\text{Fe}/\text{H}] \sim -2.4$ to $[\text{Fe}/\text{H}] \sim -1.6$ are, at fixed magnitude, systematically more metal-poor than RRab (filled symbols) variables. The trend is not very well defined in the more metal-rich ($[\text{Fe}/\text{H}] > -1.6$) and in the more metal-poor ($[\text{Fe}/\text{H}] > -2.4$) regime, due to the paucity of objects. Preliminary plain physical arguments based on the sensitivity of the HB morphology to metal content might suggest that RRc variables, being systematically hotter than RRab variables, are more associated with more metal-poor stellar populations in ω Cen. The empirical scenario is far from being fully understood, and indeed, in the *B* band, RRc and RRab variables display similar trends—when compared with the *V* band—over the entire metallicity range, thus suggesting a different sensitivity to the metal content when compared with the *V* band.

Table 2
 Mean (Metal Abundance) and Median (True Distance Modulus, Reddening) Estimates Based on REDIME (First and Second Iteration) for RRc, RRab, and Global Solution

	First Iteration			Second Iteration		
	[Fe/H] dex	μ mag	$E(B - V)$ mag	[Fe/H] dex	μ mag	$E(B - V)$ mag
RRc	$-1.98 \pm 0.06 \pm 0.53$	$13.722 \pm 0.006 \pm 0.061$	$0.124 \pm 0.013 \pm 0.028$	$-1.97 \pm 0.06 \pm 0.54$	$13.721 \pm 0.003 \pm 0.029$	$0.128 \pm 0.002 \pm 0.025$
RRab	$-1.93 \pm 0.06 \pm 0.53$	$13.711 \pm 0.004 \pm 0.042$	$0.140 \pm 0.016 \pm 0.030$	$-1.91 \pm 0.06 \pm 0.56$	$13.718 \pm 0.003 \pm 0.030$	$0.136 \pm 0.003 \pm 0.030$
Global	$-1.96 \pm 0.04 \pm 0.52$	$13.717 \pm 0.005 \pm 0.071$	$0.131 \pm 0.010 \pm 0.027$	$-1.98 \pm 0.04 \pm 0.54$	$13.720 \pm 0.002 \pm 0.030$	$0.132 \pm 0.002 \pm 0.028$

Note. The errors indicate the error on the mean/median and their standard deviation.

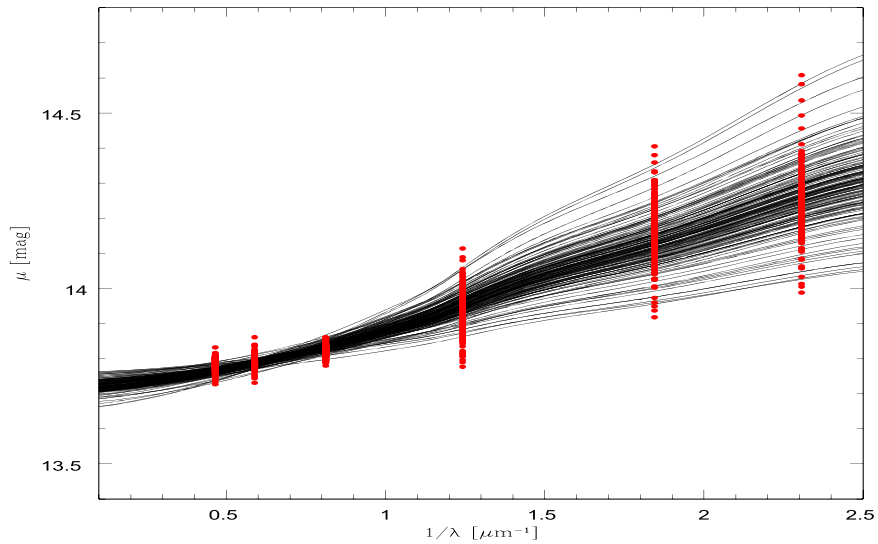


Figure 6. Same as Figure 3, but for solutions obtained in the second iteration of REDIME.

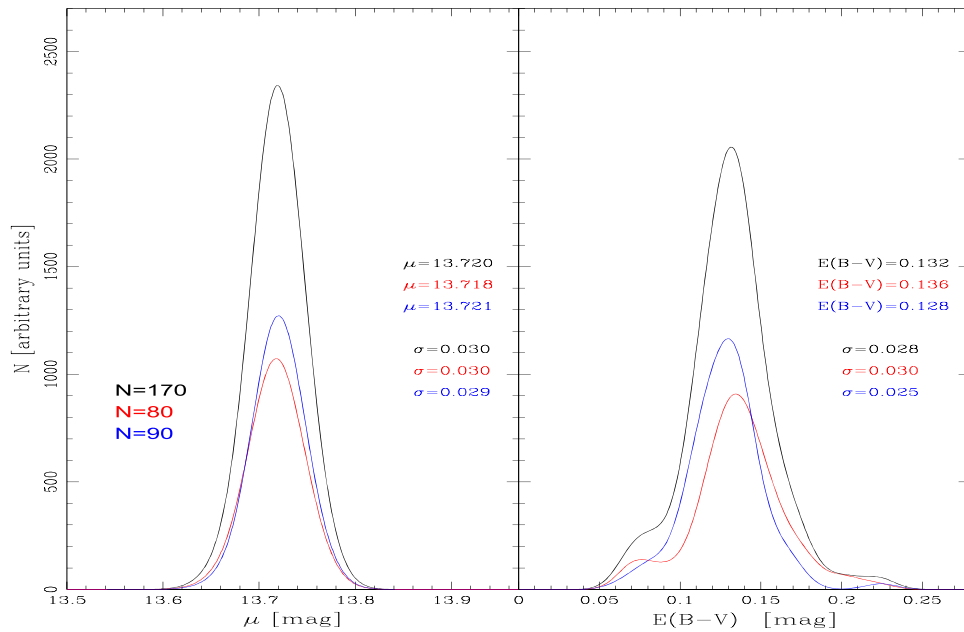


Figure 7. Same as Figure 4, but for true distance moduli and reddening estimates obtained on the second iteration of REDIME.

The internal agreement in absolute mean magnitude, reddening, and metallicity estimates is soundly supported by the optical (I) and NIR (J , H , K) data plotted in the period–luminosity plane (see Figure 9). Note that the slope is well defined for both RRc and RRab variables, and the spread in magnitude, at fixed period, is quite limited for both optical and NIR mean magnitudes.

5. Comparison with Literature Values

5.1. Metallicity Distribution

To validate the photometric metallicity estimates based on REDIME we performed a detailed comparison with similar abundance estimates available in the literature. We selected the spectroscopic sample provided by Sollima et al. (2006) and the photometric sample provided by Rey et al. (2000). To provide a homogeneous metallicity scale the iron abundances provided by

S06 and R00 were rescaled to the cluster metallicity scale provided by Carretta et al. (2009). The iron abundances by S06 were rescaled by taking into account the difference in solar iron abundance in number $\log \epsilon_{\text{Fe}} = 7.52$ versus 7.54 (Gratton et al. 2003; Carretta et al. 2009). The iron abundances by R00 were transformed from the Zinn & West (1984) metallicity scale into the Carretta et al. (2009) metallicity scale using the linear relation given in their Section 5. Moreover, the iron abundances based on the inversion of the PLZ relations were rescaled from the solar iron number abundance $\log \epsilon_{\text{Fe}} = 7.50$ adopted in pulsation (Marconi et al. 2015) and in evolutionary models (Pietrinferni et al. 2006) to 7.54 of the Carretta et al. metallicity scale.

The top panel of Figure 10 shows the comparison between the current metallicity estimates and the spectroscopic measurements provided by Sollima et al. (2006). The comparison was performed for the 67 RRLs in common in the two samples and we found that the difference is within 1σ . However, data plotted in this panel

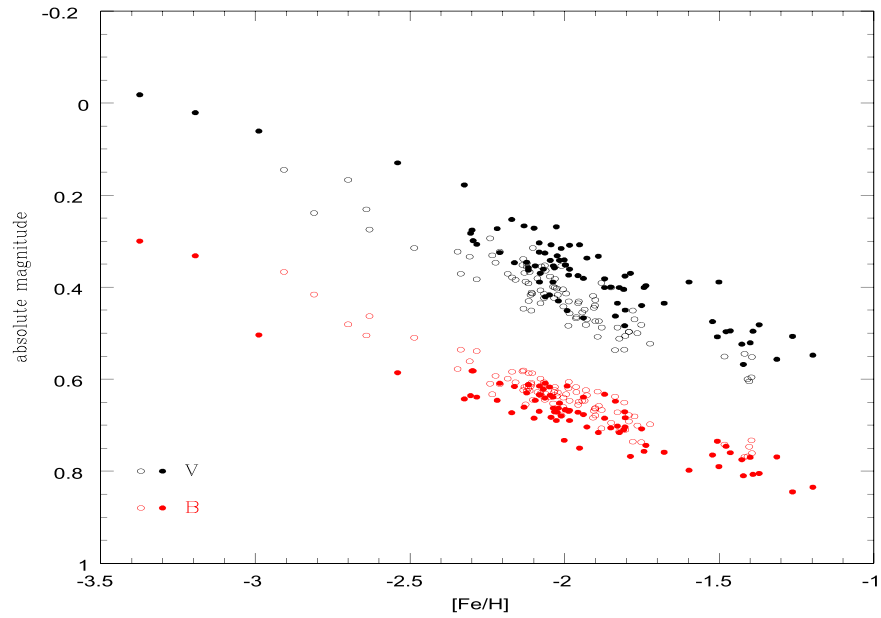


Figure 8. Absolute mean optical magnitude vs. metallicity for ω Cen RRLs. The black and red dots display B - and V -band mean magnitudes, while the filled and empty circles display fundamental (RRab) and first overtone (RRc) variables. The accuracy on the mean optical magnitudes is similar to the symbol size, and is on average better than one-hundredth of a magnitude.

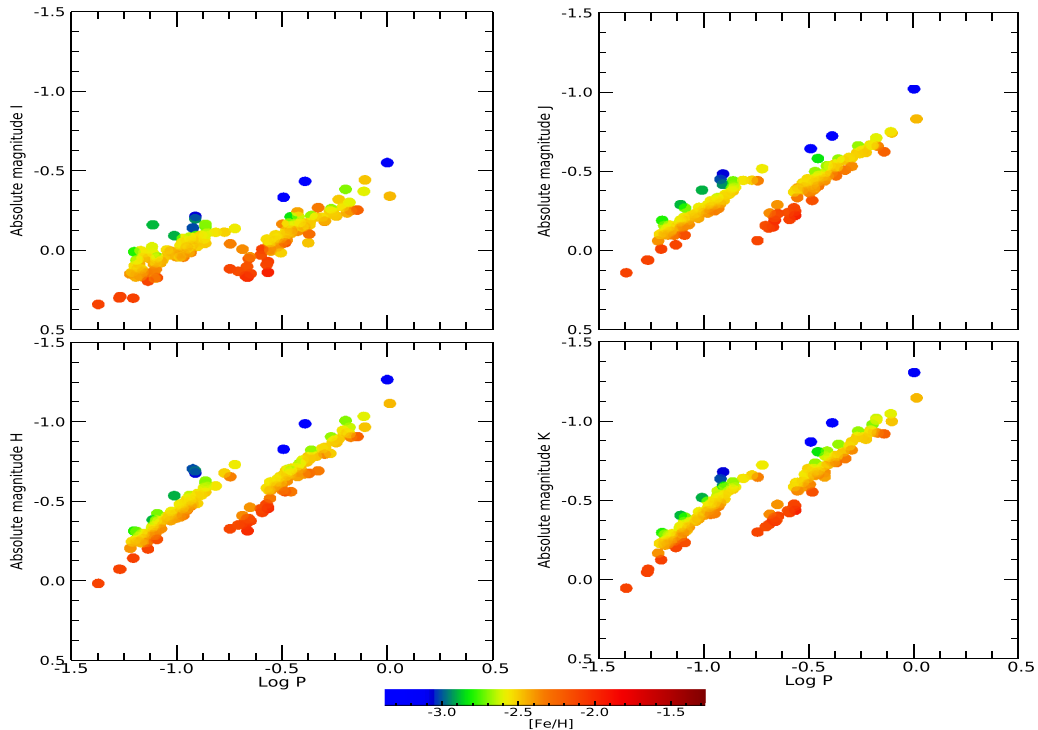


Figure 9. Period–luminosity relations for ω Cen RRLs. The color of the individual RRLs is color-coded according to their metallicity and the scale is displayed on the bottom of the figure.

display that REDIME abundances are, on average, 0.35 dex more metal-poor than the spectroscopic ones and the difference is mainly in the zero-point. The bottom panel of the same figure shows the comparison between REDIME metallicities and the photometric estimates provided by Rey et al. (2000). The comparison for the 119 RRLs in common shows the same trend already found in the comparison with the spectroscopic sample. Indeed, the difference is once again a difference in the zero-point ($\Delta[Fe/H] \approx 0.40$ dex). Data plotted in Figure 10 indicate

marginal evidence for a possible systematic trend when moving from more metal-poor to more metal-rich RRLs. However, the uncertainties on individual metallicities are still too large (see error bars) to reach a firm conclusion.

To further constrain the precision of the current metallicity scale, the left panel of Figure 11 shows a comparison between the metallicity distributions based on REDIME and the spectroscopic measurements by Sollima et al. (2006). Once again, the comparison was restricted to the 67 RRLs in common and we

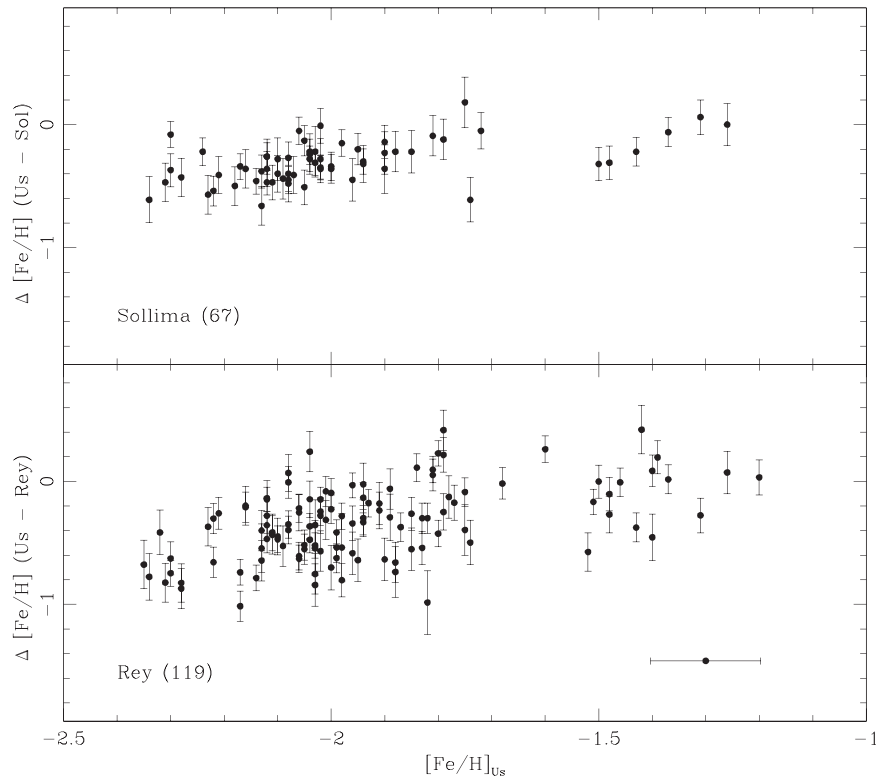


Figure 10. Top: comparison between the individual metal abundances based on REDIME and on spectroscopic measurements provided by Sollima et al. (2006). The vertical error bars display the error in quadrature of both spectroscopic and photometric errors. The error bar plotted in the bottom right corner shows the mean uncertainty on metallicity estimates based on REDIME. The number in parentheses shows the number of objects in common. Bottom: same as the top, but the comparison is with the individual metal abundances based on the spectrophotometric estimates provided by Rey et al. (2000).

found that the two distributions agree within 1σ . The distribution plotted in this panel shows that the difference is, as expected, mainly a difference in zero-point. Moreover, the standard deviation of the metallicity distribution based on REDIME abundances is 0.1 dex larger than the spectroscopic one. We have already mentioned in Section 4 that REDIME is prone to possible systematics in the zero-point of the adopted distance scale. Therefore, we performed a number of simulations to constrain this effect and we found that a decrease of 0.062 mag in the true distance modulus would provide a metallicity distribution (red dashed line) that agrees quite well with the spectroscopic distribution (see the labeled values).

We performed the same comparison with the spectrophotometric estimates provided by Rey et al. (2000). The comparison shows the same trend already found in the comparison with the spectroscopic sample. The difference is mainly in the zero-point, but the standard deviations of the two metallicity distributions are quite similar. We performed a number of simulations and we found that a decrease of 0.068 mag in the true distance modulus would provide a metallicity distribution (red dashed line) that agrees quite well with the photometric distribution (see labeled values).

The above findings indicate that we are facing two possible routes. (a) The metallicity distribution based on REDIME is ≈ 0.35 dex systematically more metal-poor than spectroscopic and spectrophotometric metallicity distributions available in the literature. (b) The current cluster true distance modulus is overestimated by 0.062 and 0.068 mag due to a systematic offset in the predicted zero-point of the RRL distance scale. Independent spectroscopic estimates covering a broader metallicity range (Chadid et al. 2017; Sneden et al. 2017) are

required to investigate whether the quoted difference is caused by uncertainties either on metallicities or on distance modulus estimates.

5.2. Reddening Distribution

We also decided to compare the RRL reddening based on REDIME with the reddening evaluations recently provided by *Gaia* DR2 (Gaia Collaboration et al. 2018). The reason why we decided to use the reddening given in the general source catalog instead of the reddening provided for the RRLs is twofold.

(i). The number of ω Cen RRLs present in the *Gaia* catalog for variable stars is quite limited (97 out of 198). Moreover, the light curves and the pulsation parameters are not very accurate due to crowding and phase coverage problems.

(ii). To properly evaluate the reddening distribution across the body of the cluster we first selected in the *Gaia* source catalog the candidate cluster stars using the new proper motion measurements. We plotted all the ω Cen sources within the truncation radius of ω Cen ($r_t = 57.03$ arcmin; Harris 1996 and updates). Candidate cluster stars were identified as a secondary maximum in the proper motion plane with a centroid located at $\mu_{\alpha*} = -3.18$ mas yr $^{-1}$ and $\mu_\delta = -6.72$ mas yr $^{-1}$. Note that the current estimates agree quite well with the proper motion estimate ($\mu_{\alpha*} = -3.1925 \pm 0.0022$ mas yr $^{-1}$, $\mu_\delta = -6.7445 \pm 0.0019$ mas yr $^{-1}$) provided by *Gaia* DR2 (Gaia Collaboration et al. 2018). The stars brighter than $G = 16.5$ mag located within 1.16 mas yr $^{-1}$ of the centroid position were considered candidate cluster stars. We plotted this sample in a 3D magnitude-color-color plot— G , GBP—GRP—and we

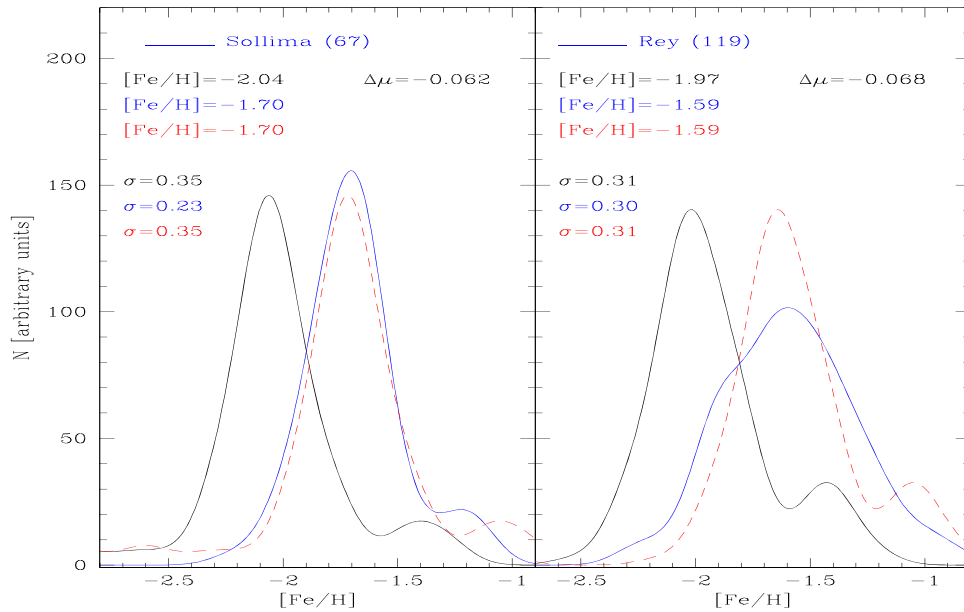


Figure 11. Left: comparison between the metallicity distribution based on REDIME (black line) and on spectroscopic measurements (blue line) for RRLs provided by Sollima et al. (2006). The dashed red line shows the metallicity distribution based on RRLs once we assume a true distance modulus that is 0.062 mag fainter than the true distance modulus based on REDIME. The peaks, the standard deviations of the different metallicity distributions, and the number of objects in common are also labeled. Right: same as the left, but the comparison is with the metallicity distribution based on spectrophotometric measurements provided by Rey et al. (2000).

selected the stars belonging to the ω Cen cluster sequences. We ended up with a sample of ~ 3700 stars and we found that the $E(GBP-GRP)$ is centered on 0.117 mag and the standard deviation is $\sigma = 0.088$ mag. Note that in performing this fit we neglected the very high reddening tail of the distribution ($E(GBP-GRP) > 0.3$ mag).

To compare the reddening distribution based on RRLs and on *Gaia* estimates, we transformed the $E(B-V)$ into $E(GBP-GRP)$ using the Cardelli’s empirical reddening law and the following extinction coefficients: $A_G/A_V = 0.840$ mag, $A_{BP}/A_V = 1.086$ mag, and $A_{RP}/A_V = 0.627$ mag.²⁵ The reddening in the *Gaia* source catalog was estimated using the spectral energy distribution of individual sources. The interstellar absorption in the *Gaia* Source catalog was estimated using the three photometric bands (G , G_{BP} , G_{RP}) and the parallax. The approach relies on the application of a machine-learning algorithm to a training data set that includes stars characterized by low extinctions and for which the effective temperature was typically spectroscopically estimated (see Section 2.1 in Andrae et al. (2018)). We found that the reddening distribution is centered on 0.115 mag, and the standard deviation is $\sigma = 0.065$ mag. The two independent reddening distributions are in reasonable agreement, in particular, if we account the difference in sample size (170 versus 3700), in spatial distribution, and in the adopted photometric system.

To further investigate the reddening variation across the field of view, we plotted the spatial distribution of RRLs investigated with REDIME on sky (see the left panel of Figure 12). The reddening is color-coded and the scale is displayed on the bottom. To overcome the limitation of discrete sampling, the reddening map was computed using a bidimensional grid with a bin of ~ 2.5 arcsec. The reddening of individual grid points was estimated by averaging the

reddening of RRLs in the entire sample according to the radial distance between the grid point and all the RRLs in our sample. The closer the RRL, the larger its contribution to the mean reddening of the grid point. We followed this approach to estimate the reddening map, because it naturally smoothes the reddening distribution in the cluster regions covered by RRLs.

The reddening map shown in the left panel of Figure 12 indicates that the largest variations are across the second and third quadrants (X from -5 to -10 arcmin, Y from -5 to 12 arcmin) in which the reddening changes from a few hundredths of a magnitude to a few tenths of a magnitude ($E(B-V) \sim 0.25$ mag). These findings further support the evidence that the extinction toward ω Cen changes on spatial scales of the order of a few arcminutes or even less. Moreover, there is no clear evidence of a radial extinction gradient in the cluster region covered by the current sample. The lack of a gradient either in reddening and/or in metal abundance should be cautiously treated, since we are missing the RRLs located on the outskirts of the cluster (Fernández-Trincado et al. 2015).

To further investigate the reddening variation across the body of the cluster, the right panel of the same figure shows the map based on reddening estimates provided by *Gaia* DR2. Note that to properly compare the two samples for each RRL, we only selected the closest static star in the *Gaia* source catalog. The two reddening maps display similar variations. There is no clear evidence of an extinction gradient and the spatial variations of the reddening are quite similar to the map based on RRLs. Moreover, the mean reddening of the 170 static stars is 0.107 mag and its standard deviation is 0.055 mag. The difference between the estimates based on the entire sample (3700 sources) is minimal concerning the mean reddening (0.107 versus 0.115), but the standard deviation decreases from 0.065 to 0.055 mag. The new standard deviation is still larger than the standard deviation based on RRLs (0.28 mag). The difference is mainly caused by the limited sample of stars in the *Gaia* source catalog located in the innermost regions of the cluster due to the extreme crowding.

²⁵ We adopted the new measurements of the *Gaia* passbands provided by Evans et al. (2018) and performed a polynomial fit to estimate the central wavelengths. We found $\lambda_c(G) \sim 6420$ Å, $\lambda_c(GBP) \sim 5130$ Å, $\lambda_c(GRP) \sim 7800$ Å.

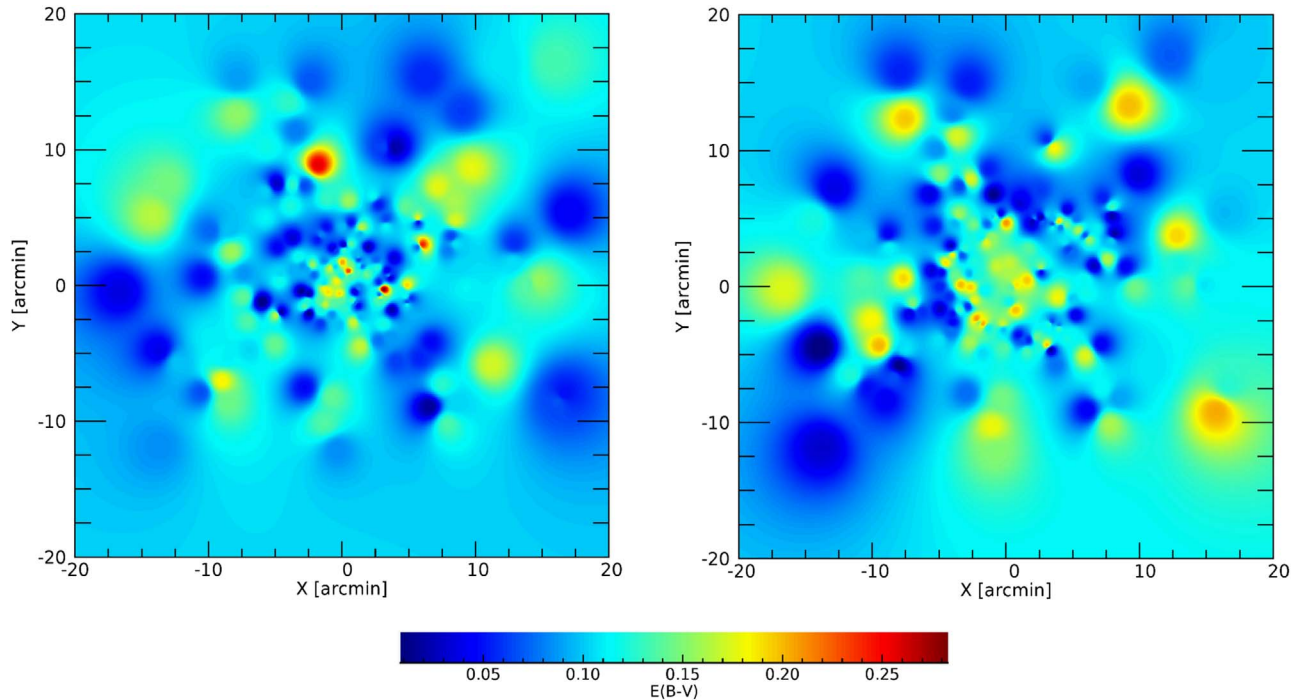


Figure 12. Left: reddening distribution across the body of ω Cen. The individual mean reddening estimates are based on REDIME and are color-coded according to the reddening value (scale on the bottom). The reddening distribution was estimated using the relative RRL distance (see the text for more details). Right: same as the left, but the reddening distribution was estimated using reddening estimates provided by *Gaia* DR2 (Gaia Collaboration et al. 2018). To avoid possible systematics in the reddening distribution, cluster stars were selected according to radial distance and proper motion. Moreover, to compare two samples with similar spatial distributions for each RRL in our sample, we only selected the closest static star.

5.3. True Distance Modulus Distribution

Data plotted in Figure 13 display the comparison between recent estimates of both true distance modulus and reddening to ω Cen. Note that we decided to use this plane, since absolute distance estimates available in the literature are typically correlated either with the estimate of the cluster reddening or with the adopted cluster reddening and/or with the adopted reddening law.

The mean over the literature values are (for more details see Table 3): $\mu = 13.690 \pm 0.018$ (error on the mean) ± 0.063 (standard deviation) mag and $E(B - V) = 0.118 \pm 0.003$ (error on the mean) ± 0.016 (standard deviation) mag. The dashed blue box shows the 1σ region in μ and in $E(B - V)$, while the red point and the red lines display the REDIME estimates and their standard deviations. Note that in several of the quoted papers the authors do not provide an error concerning the estimated/adopted cluster reddening. We adopted for these estimates a conservative error of 0.01 mag.

There is evidence that the current true distance modulus is a few hundredths of a magnitude larger than suggested in the literature. The same outcome also applies to the current estimate of the mean cluster reddening that is ~ 0.01 mag larger than the literature values. However, both the cluster true distance modulus and the cluster reddening agree within 1σ .

6. Summary and Final Remarks

We took advantage of the accurate and homogeneous optical (*BVI*) and NIR (*JHK*) mean magnitudes for RRLs in ω Cen to develop a new algorithm (REDIME) to fully exploit the use of RRLs as distance indicators and tracers of old stellar populations. The main reason we selected ω Cen is because its stellar content is affected by a well known spread in metal

content (Johnson & Pilachowski 2010). Moreover, there is evidence of a mild variation in cluster reddening when moving across the body of the cluster. This means that ω Cen is a solid laboratory to evaluate the accuracy of the intrinsic parameters (distance, metallicity, reddening) for individual RRLs.

We found that we cannot solve simultaneously for the three unknown parameters (distance, metallicity, reddening) because the adopted optical and NIR mean magnitudes display similar metallicity dependencies. This is the reason why we developed a new algorithm (REDIME) based on two steps. In the first step, we took advantage of the theoretical and empirical evidence that the $V, B - I$ period–Wesenheit relation for RRLs is minimally affected by the metallicity. On the basis of this individual estimates of the metallicity we provided a preliminary estimate of the cluster distance and of the cluster reddening using the same approach adopted by Inno et al. (2016) for Large Magellanic Cloud Cepheids. In the second step, we used the NIR (*J, H, K*) PL relations to provide new individual metallicity estimates together with optical and NIR mean magnitudes to simultaneously estimate true distance modulus and cluster reddening. The main results of our approach are the following:

(i) Metallicity distribution—the metallicity distribution shows a well defined peak at $[\text{Fe}/\text{H}] = -1.98 \pm 0.04$. The spread in iron abundance is of the order of 0.54 dex and it is intrinsic, i.e., it is not dominated by uncertainties on individual measurements. There is evidence of a metal-intermediate group of RRLs located at $[\text{Fe}/\text{H}] \sim -1.5$ together with a minor tail of very metal-poor ($[\text{Fe}/\text{H}] \leq -2.3$) objects. The comparison with metallicity distributions available in the literature shows that the current distribution is systematically more metal-poor than the spectroscopic measurements (67 objects in common) provided by Sollima et al. (2006) and with the spectrophotometric

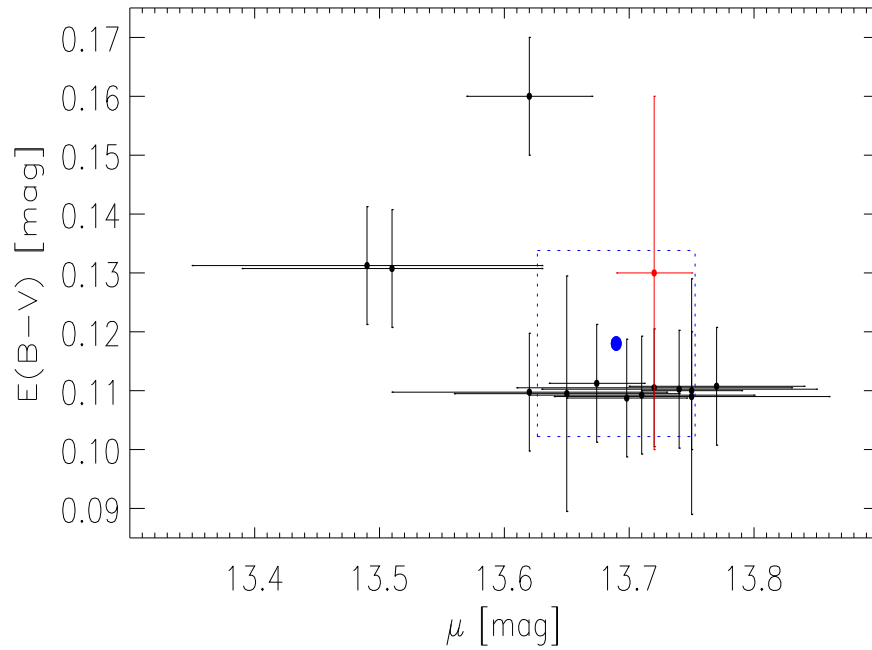


Figure 13. Comparison between cluster reddening vs. cluster true distance modulus for ω Cen based either on REDIME (red point) or available in the literature (black points; see also Table 3). The red and the black lines display either the standard deviation of the distributions or the error bars. The blue dashed lines display the 1σ box and the mean (blue circle) of all the measurements.

measurements (119 objects in common) provided by Rey et al. (2000). The differences are of the order of 0.3 dex (1σ). In this context it is worth mentioning that a systematic error of the order of -0.06 , -0.07 mag in the cluster true distance modulus, based on predicted PLZ and mean magnitude–metallicity relations, would enable quite good agreement between the current metallicity distribution and similar distributions available in the literature. The spectroscopic sample is only based on 67 RRLs; it is clear that larger and homogeneous samples are mandatory to further support a spectroscopic route to determining the accuracy and precision of the true distance modulus.

(ii) True distance modulus distribution—the true distance moduli we estimated for the RRC, RRab, and global sample agree quite well with each other and the mean is $\mu = 13.720 \pm 0.002 \pm 0.030$ mag. The quoted errors do not account for uncertainties in the zero-point. Note that the accuracy of the current cluster true distance modulus mainly depends on the NIR bands (J , H , K), since the slope of both PL and PW relations increases, while the standard deviation decreases when moving toward longer wavelengths. In passing, we also note that REDIME relies on multiple optical and NIR mean magnitudes. This means that REDIME simultaneously takes account of the optical/NIR intrinsic color variation of RRLs.

The accuracy of the five field RRLs for which the trigonometric parallax was measured using the Fine Guide Sensor on board the *Hubble Space Telescope* does not allow us to improve the current RRL distance scale. It is clear that *Gaia* is going to play a crucial role in this issue, because the number of RRLs for which the trigonometric parallax is going to have an accuracy better than $1 \mu\text{as}$ is two/three orders of magnitude larger than the current ones. However, only a minor fraction of them have already iron abundances based on high resolution spectra (Chadid et al. 2017; Magurno et al. 2018). The bulk of metallicity estimates of field RRLs are still based either on

medium-resolution spectra or on the ΔS method (Layden 1994; Kinman et al. 2012; Sesar et al. 2013; Dambis et al. 2014; Sesar et al. 2017; M. Fabrizio et al. 2018, in preparation). These metal abundances have been recently used by Muraveva et al. (2018) together with the optical, near-/mid-infrared magnitudes available in the literature and trigonometric parallaxes by *Gaia* DR2. They provided new period–luminosity–metallicity relations and found that the current parallaxes are affected by a zero-point offset of -0.057 mas. These finding supports previous investigations by Arenou et al. (2018) and by Sesar et al. (2017).

The *Gaia* DR2 parallaxes are systematically smaller than expected. This systematic error is known, it depends on several parameters (sky distribution, distance color, number of measurements), and it is ~ -0.029 mas when compared with the positions of more than 500,000 active galactic nuclei (Lindgren et al. 2018). In this context it is worth mentioning that similar analyses, but based on different stellar tracers, provide zero-point offsets similar to those of RRLs (classical Cepheids ~ -0.046 mas, Riess et al. 2018 ~ -0.049 mas, Groenewegen 2018; red giants observed by KEPLER ~ -0.053 mas, Zinn et al. 2018). This circumstantial evidence indicates that the near future scenario is very promising, but we need a few more years to nail down systematics in trigonometric distances.

Note that *Gaia* is also going to provide metallicity estimates based either on spectroscopy or spectrophotometry for variable stars, but a significant sample cannot be anticipated until DR4. The brightest RRL is the prototype RR Lyr itself ($m_V = 7.68$ mag) and they become fainter than $m_V \sim 20$ –21 mag in the outskirts of the Galactic Halo.

(iii) Reddening distribution—we found that the cluster reddening distribution based on RRC, RRab, and the global sample agree quite well with each other and the mean is $E(B - V) = 0.132 \pm 0.002 \pm 0.028$ mag. The standard deviations of the three distributions are also quite similar, with the

Table 3
True Distance Moduli and Reddening for ω Cen Available in the Literature

μ mag	$E(B - V)^a$ mag	References	Notes ^b
13.36 \pm 0.10	0.11 ^c	Cannon & Kontizas (1974)	(1)
13.61	0.11 (Buonanno et al. 1989)	Longmore et al. (1990)	(2)
13.53 \pm 0.20	0.11 ^d	Nemec et al. (1994)	(3)
14.02 \pm 0.10	0.12 ^d	McNamara (2000)	(4)
13.74 \pm 0.11	0.11 ^c	Caputo et al. (2002)	(5)
13.75 \pm 0.04	0.11 ^c	Kaluzny et al. (2002)	(6)
13.72 \pm 0.11	0.11 \pm 0.01 (Calamida et al. 2005)	Del Principe et al. (2006)	(7)
13.62 \pm 0.11	0.11 \pm 0.01 (Calamida et al. 2005)	Del Principe et al. 2006	(7)
13.77 \pm 0.07	0.11 \pm 0.01 (Calamida et al. 2005)	Del Principe et al. (2006)	(8)
13.72	0.11 \pm 0.01 (Ferraro et al. 1999)	Sollima et al. (2006)	(9)
13.49 \pm 0.14	0.13 (Schlegel et al. 1998)	(Kaluzny et al. 2007)	(10)
13.51 \pm 0.12	0.13 (Schlegel et al. 1998)	(Kaluzny et al. 2007)	(10)
13.68 \pm 0.27	0.12 (Harris 1996)	Weldrake et al. (2007)	(11)
13.65 \pm 0.09	0.11 \pm 0.02 (Calamida et al. 2005)	Bono et al. (2008)	(12)
13.75 \pm 0.11	0.11 \pm 0.02 (Calamida et al. 2005)	Bono et al. (2008)	(13)
13.62 \pm 0.05	0.16	McNamara (2011)	(14)
13.71 \pm 0.08	0.11 (Thompson et al. 2001; Lub 2002)	Braga et al. (2016)	(15)
13.65 \pm 0.08	0.12 (Harris 1996)	Bhardwaj et al. (2017)	(16)
13.77 \pm 0.08	0.12 (Harris 1996)	Bhardwaj et al. (2017)	(16)
13.70 \pm 0.11	0.12 (Harris 1996)	Bhardwaj et al. (2017)	(16)
13.708 \pm 0.035	0.12 (Harris 1996)	Navarrete et al. (2017)	(17)
13.674 \pm 0.038	0.11 (Thompson et al. 2001; Lub 2002)	Braga et al. (2018)	(18)
13.698 \pm 0.048	0.11 (Thompson et al. 2001; Lub 2002)	Braga et al. (2018)	(18)
13.720 \pm 0.002 \pm 0.030	0.132 \pm 0.002 \pm 0.028	This work	(19)

Notes.

^a The reddening estimates, $E(B-V)$, derived by the authors of the investigation are marked in bold. For the investigations in which the reddening was assumed from the literature, we include the reference.

^b (1) Distance based on the visual band, M_V , of the horizontal branch. (2) Distance based on the K -band PL relation. The relation was calibrated using $M_{K,0,-0.3} = 0.06$ and $[\text{Fe}/\text{H}] = -0.24$. (3) Distance based on the $B_{0,-0.3}$, $V_{0,-0.3}$, and $K_{0,-0.3}$ magnitudes of RRLs, where the subscript 0, -0.3 means the reddening-corrected magnitude at $\log P = -0.3$. (4) Distance based on the V -band PL relation of high-amplitude δ Sct stars. (5) Distance based on the position of the first overtone blue edge of the instability strip in the $\log P - M_V$ diagram. (6) Distance based on the surface brightness method, applied to the detached eclipsing binary V212 to derive the absolute distance to ω Cen. (7) Distance based on the $M_V - [\text{Fe}/\text{H}]$ relation, calibrated with Bono et al. (2003) and with Catelan (2006) for the two values. (8) Distance based on the semi-empirical calibration of the K_s -band PL relation by Bono et al. (2003). (9) Distance based on a new calibration of the K_s -band PL relation. The zero-point was based on the trigonometric parallax of the prototype RR Lyr (Benedict et al. 2011). (10) Distance based on the orbital parameters of the detached eclipsing binary V209. The two distance moduli are for the primary (closest) and for the secondary (farthest) star of the binary system. (11) Distance based on the $M_V - [\text{Fe}/\text{H}]$ relation, calibrated with Rich et al. (2005). (12) Distance based on the calibration of the TRGB provided by Lee et al. (1993). (13) Distance based on the empirical K -band PL relation provided by (Sollima et al. 2008). (14) Distance based on the V -band PL relation of δ Sct stars. (15) Distance based on semi-empirical and theoretical calibration of the reddening independent $PW(V, B-I)$ relations. (16) Distance based on the the J -, H -, and K -band PL relations of Type II Cepheids (T2Cs), based on a new calibration of the Large Magellanic Cloud Type II Cepheids. (17) Distance based on the J - and K -band PL relations of both RRLs and Type II Cepheids, calibrated with the relations of (Alonso-García et al. 2015). (18) Distance based on the J -, H -, and K_s -band PLZ relations of RRLs, calibrated with the predicted relations and adopting $[\text{Fe}/\text{H}]$ from Sollima et al. (2006) and Braga et al. (2016). $E(B-V)$ from (Thompson et al. 2001; Lub 2002). (19) Distance and reddening based on the application of REDIME to the $BVIJHK_s$ mean magnitudes of RRLs.

^c The authors provide apparent distance modulus $(m - M)_V$ and not the true distance modulus μ . Therefore, we adopt $E(B - V) = 0.11$ (Thompson et al. 2001; Lub 2002) and provide μ in column 1.

^d The authors do not quote the paper from which the reddening value was adopted.

distribution based on RRc being slightly narrower and more symmetric. The accuracy of the current reddening estimates mainly relies on optical bands (BVI), with the NIR (JHK) bands playing a minor role, since the slope of the reddening law is quite constant in this wavelength regime. The current cluster reddening estimates agree quite well with similar estimates recently provided by *Gaia*. We also found that the reddening changes by more than a factor of two on spatial scales of the order of arcminutes. The quoted cluster true distance modulus and cluster reddening agree within 1σ with similar estimates available in the literature.

(iv) Metallicity dependence—preliminary empirical evidence suggests the expected correlation between optical magnitudes (B , V) and metal content. The current sample

cover more than 1.5 dex and the difference in magnitude is roughly half a magnitude. The same outcome applies to the PL relations, but the impact of the metal content at fixed period is, as expected, milder.

REDIME is a promising approach for constraining the intrinsic parameters of both field and cluster RRLs. This working hypothesis is further strengthened by the evidence that REDIME provides accurate estimates of metallicity, true distance modulus, and reddening for Blazkho RRLs once accurate optical/NIR mean magnitudes are available. In passing we note that 26 out of the 170 RRLs adopted in this investigation are candidate Blazkho RRLs. The improvement of individual distances provides the opportunity to improve the accuracy of both metal content, reddening, and possibly helium

content (Marconi et al. 2018). New and accurate spectroscopic measurements together with *Gaia* parallaxes will provide an opportunity to calibrate new optical/NIR PLZ and PWZ relations, and in turn, the opportunity to apply REDIME in Local Group galaxies.

It goes without saying that REDIME was also developed to take advantage of the time series in six (*ugrizy*) different bands that will be collected by LSST for resolved stellar populations in Local Group and in Local Volume galaxies (Ivezić et al. 2012). There are solid reasons to believe that this photometric system is going to provide very accurate reddenings and metallicity estimates, but detailed simulations are required to characterize this photometric system for RRLs. Solid clues regarding the accuracy of the LSST photometric system in constraining metallicity, true distance modulus, and reddening can also be derived using the multi-band, multi-epoch DECam images for cluster (Vivas et al. 2017) and Bulge (Saha & Vivas 2017) RRLs with the key advantage of covering the entire body of the cluster with a single or at most a few pointings (Calamida et al. 2017).

It is a real pleasure to thank the anonymous referee for their positive opinion concerning the content and the cut of this investigation, in particular, for their constructive suggestions that improved the readability of the paper. This investigation was partially supported by PRIN-INAF 2016 ACDC (P.I.: P. Caraveo). M.M. was partially supported by NSF grant

AST-1714534. This work has made use of data from the European Space Agency (ESA) mission *Gaia* (<https://www.cosmos.esa.int/gaia>), processed by the *Gaia* Data Processing and Analysis Consortium (DPAC, <https://www.cosmos.esa.int/web/gaia/dpac/consortium>). Funding for the DPAC has been provided by national institutions, in particular the institutions participating in the *Gaia* Multilateral Agreement. This research has made use of the GaiaPortal catalogs access tool, ASI—Space Science Data Center, Rome, Italy (<http://gaiaportal.ssd.cnr.it>). We would also like to acknowledge the financial support of INAF (Istituto Nazionale di Astrofisica), Osservatorio Astronomico di Roma, ASI (Agenzia Spaziale Italiana) under contract to INAF: ASI 2014-049-R.0 dedicated to SSDC. This publication makes use of data products from the Two Micron All Sky Survey, which is a joint project of the University of Massachusetts and the Infrared Processing and Analysis Center/California Institute of Technology, funded by the National Aeronautics and Space Administration and the National Science Foundation. This research has made use of the USNO Image and Catalogue Archive operated by the United States Naval Observatory, Flagstaff Station (<http://www.nofs.navy.mil/data/fchpix/>). This research has made use of NASA’s Astrophysics Data System.

Appendix

Flow Chart of REDIME’s Algorithm

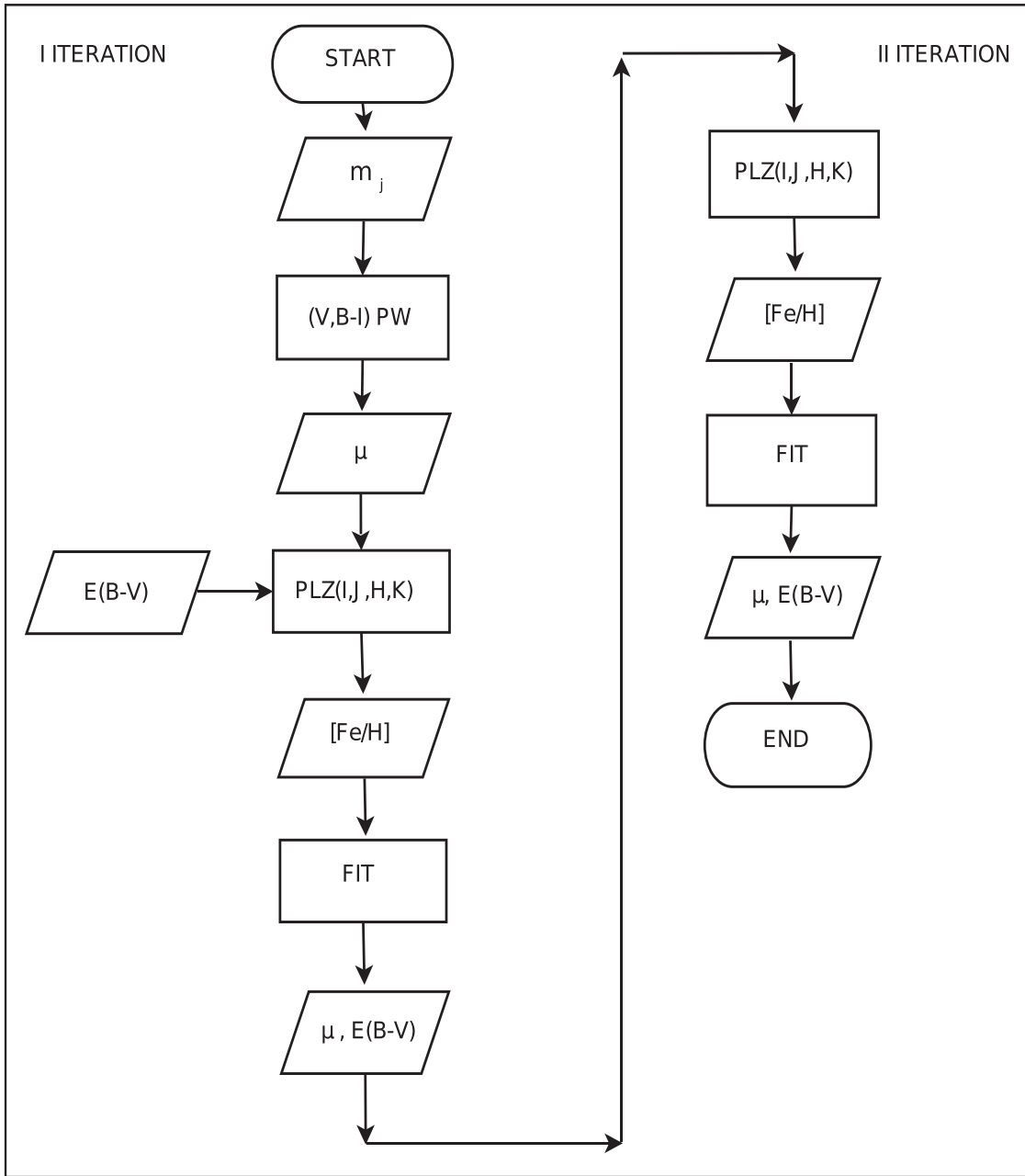


Figure 14. Left: flow chart of the first iteration of REDIME’s algorithm. The algorithm is based on the six mean magnitudes available for RRLs in our sample and the use of the optical $(V, B - I)$ PW relation to provide the first estimate of the ω Cen true distance modulus. The new distance and the mean cluster reddening available in the literature are used to provide four independent estimates of the iron abundance using the PLZ relations in the I, J, H, K bands and Equation (1). The mean metallicity for each RRL in the sample is estimated as the mean of the estimates based on NIR (JHK) PLZ relations. The new mean metallicity is used to provide new simultaneous estimates of the true distance modulus and reddening using four (JHK) PLZ relations, two $MZ (BV)$ relations, and the nonlinear fit with the assumed reddening law (Equation (2)). Right: the output of the first iteration, namely the true distance modulus and the reddening are now used as an input for the second iteration. The four JHK PLZ relations are used once again to provide new iron abundances. The new mean value based on NIR PLZ relations is used to provide the final simultaneous estimates of both the true distance modulus and the reddening using the nonlinear fit dictated by Equation (2).

ORCID iDs

G. Bono <https://orcid.org/0000-0002-4896-8841>
 V. F. Braga <https://orcid.org/0000-0001-7511-2830>
 P. B. Stetson <https://orcid.org/0000-0001-6074-6830>
 D. Magurno <https://orcid.org/0000-0001-5479-5062>
 R. L. Beaton <https://orcid.org/0000-0002-1691-8217>
 B. Chaboyer <https://orcid.org/0000-0003-3096-4161>
 M. Dall’Ora <https://orcid.org/0000-0001-8209-0449>
 M. Fabrizio <https://orcid.org/0000-0001-5829-111X>

G. Fiorentino <https://orcid.org/0000-0003-0376-6928>
 B. F. Madore <https://orcid.org/0000-0002-1576-1676>
 M. Marengo <https://orcid.org/0000-0001-9910-9230>
 C. E. Martinez-Vazquez <https://orcid.org/0000-0002-9144-7726>
 M. Monelli <https://orcid.org/0000-0001-5292-6380>
 J. R. Neeley <https://orcid.org/0000-0002-8894-836X>
 C. Sneden <https://orcid.org/0000-0002-3456-5929>

E. Valenti  <https://orcid.org/0000-0002-6092-7145>A. R. Walker  <https://orcid.org/0000-0002-7123-8943>

References

- Alonso-García, J., Dékány, I., Catelan, M., et al. 2015, *AJ*, 149, 99
- Andrae, R., Fouesneau, M., Creevey, O., et al. 2018, *A&A*, 616, A8
- Arenou, F., Luri, X., Babusiaux, C., et al. 2018, *A&A*, 616, A17
- Baade, W. 1956, *PASP*, 68, 5
- Benedict, G. F., McArthur, B. E., Feast, M. W., et al. 2011, *AJ*, 142, 187
- Bhardwaj, A., Macri, L. M., Rejkuba, M., et al. 2017, *AJ*, 153, 154
- Bono, G., Caputo, F., Castellani, V., et al. 2003, *MNRAS*, 344, 1097
- Bono, G., Marconi, M., & Stellingwerf, R. F. 1999, *ApJS*, 122, 167
- Bono, G., & Stellingwerf, R. F. 1994, *ApJS*, 93, 233
- Bono, G., Stetson, P. B., Sanna, N., et al. 2008, *ApJL*, 686, L87
- Braga, V. F., Dall’Ora, M., Bono, G., et al. 2015, *ApJ*, 799, 165
- Braga, V. F., Stetson, P. B., Bono, G., et al. 2016, *AJ*, 152, 170
- Braga, V. F., Stetson, P. B., Bono, G., et al. 2018, *AJ*, 155, 137
- Buonanno, R., Corsi, C. E., & Fusi Pecci, F. 1989, *A&A*, 216, 80
- Calamida, A., Stetson, P. B., Bono, G., et al. 2005, *ApJL*, 634, L69
- Calamida, A., Strampelli, G., Rest, A., et al. 2017, *AJ*, 153, 175
- Campbell, M. A., Evans, C. J., Mackey, A. D., et al. 2010, *MNRAS*, 405, 421
- Cannon, R. D., & Kontizas, M. 1974, *MNRAS*, 167, 51P
- Caputo, F., degl’Innocenti, S., & Marconi, M. 2002, in ASP Conf. Ser. 265, Omega Centauri, A Unique Window into Astrophysics, ed. F. van Leeuwen, J. D. Hughes, & G. Piotto (San Francisco, CA: ASP), 185
- Cardelli, J. A., Clayton, G. C., & Mathis, J. S. 1989, *ApJ*, 345, 245
- Carretta, E., Bragaglia, A., Gratton, R., D’Orazi, V., & Lucatello, S. 2009, *A&A*, 508, 695
- Catelan, M. 2006, *RMxAA*, 27, 93
- Catelan, M., Pritzl, B. J., & Smith, H. A. 2004, *ApJS*, 154, 633
- Chadid, M., Sneden, C., & Preston, G. W. 2017, *ApJ*, 835, 187
- Coppola, G., Marconi, M., Stetson, P. B., et al. 2015, *ApJ*, 814, 71
- Dambis, A. K., Rastorguev, A. S., & Zabolotskikh, M. V. 2014, *MNRAS*, 439, 3765
- Del Principe, M., Piersimoni, A. M., Storm, J., et al. 2006, *ApJ*, 652, 362
- Evans, D. W., Riello, M., De Angeli, F., et al. 2018, *A&A*, 616, A4
- Fernández-Trincado, J. G., Vivas, A. K., Mateu, C. E., et al. 2015, *A&A*, 574, A15
- Ferraro, F. R., Messineo, M., Fusi Pecci, F., et al. 1999, *AJ*, 118, 1738
- Feuchtinger, M. U. 1999, *A&A*, 351, 103
- For, B.-Q., Sneden, C., & Preston, G. W. 2011, *ApJS*, 197, 29
- Gaia Collaboration, Brown, A. G. A., Vallenari, A., et al. 2018, *A&A*, 595, A2
- Gratton, R. G., Carretta, E., Claudi, R., Lucatello, S., & Barbieri, M. 2003, *A&A*, 404, 187
- Groenewegen, M. A. T. 2018, arXiv:1808.05796
- Harris, W. E. 1996, *AJ*, 112, 1487
- Hubble, E. P. 1925, *Obs*, 48, 139
- Hughes, J., & Wallerstein, G. 2000, *AJ*, 119, 1225
- Inno, L., Bono, G., Matsunaga, N., et al. 2016, *ApJ*, 832, 176
- Ivezić, Ž., Beers, T. C., & Jurić, M. 2012, *ARA&A*, 50, 251
- Johnson, C. I., & Pilachowski, C. A. 2010, *ApJ*, 722, 1373
- Kaluzny, J., Rucinski, S. M., Thompson, I. B., Pych, W., & Krzeminski, W. 2007, *AJ*, 133, 2457
- Kaluzny, J., Thompson, I., Krzeminski, W., et al. 2002, in ASP Conf. Ser. 265, Omega Centauri, A Unique Window into Astrophysics, ed. F. van Leeuwen, J. D. Hughes, & G. Piotto (San Francisco, CA: ASP), 155
- Kinman, T. D., Cacciari, C., Bragaglia, A., Smart, R., & Spagna, A. 2012, *MNRAS*, 422, 2116
- Kovacs, G., Kisvarsanyi, E. G., & Buchler, J. R. 1990, *ApJ*, 351, 606
- Layden, A. C. 1994, *AJ*, 108, 1016
- Leavitt, H. S. 1908, *AnHar*, 60, 87
- Lee, M. G., Freedman, W., Mateo, M., et al. 1993, *AJ*, 106, 1420
- Lindgren, L., Hernández, J., Bombrun, A., et al. 2018, *A&A*, 616, A2
- Longmore, A. J., Dixon, R., Skillen, I., Jameson, R. F., & Fernley, J. A. 1990, *MNRAS*, 247, 684
- Longmore, A. J., Fernley, J. A., & Jameson, R. F. 1986, *MNRAS*, 220, 279
- Lub, J. 2002, in ASP Conf. Ser. 265, Omega Centauri, A Unique Window into Astrophysics, ed. F. van Leeuwen, J. D. Hughes, & G. Piotto (San Francisco, CA: ASP), 95
- Madore, B. F., Welch, D. L., McAlary, C. W., & McLaren, R. A. 1987, *ApJ*, 320, 26
- Magurno, D., Sneden, C., Braga, V. F., et al. 2018, *ApJ*, 864, 57
- Marconi, M., Bono, G., Pietrinferni, A., et al. 2018, arXiv:1808.07348
- Marconi, M., Coppola, G., Bono, G., et al. 2015, *ApJ*, 808, 50
- Martínez-Vázquez, C. E., Monelli, M., Gallart, C., et al. 2016, *MNRAS*, 461, L41
- McNamara, D. H. 2000, *PASP*, 112, 1096
- McNamara, D. H. 2011, *AJ*, 142, 110
- Muraveva, T., Delgado, H. E., Clementini, G., Sarro, L. M., & Garofalo, A. 2018, *MNRAS*, arXiv:1805.08742
- Navarrete, C., Catelan, M., Contreras Ramos, R., et al. 2017, *A&A*, 604, A120
- Nemec, J. M., Nemeč, A. F. L., & Lutz, T. E. 1994, *AJ*, 108, 222
- Pancino, E., Britavskiy, N., Romano, D., et al. 2015, *MNRAS*, 447, 2404
- Pietrinferni, A., Cassisi, S., Salaris, M., & Castellì, F. 2006, *ApJ*, 642, 797
- Rey, S.-C., Lee, Y.-W., Joo, J.-M., Walker, A., & Baird, S. 2000, *AJ*, 119, 1824
- Rich, J. A., Persson, S. E., Freedman, W. L., et al. 2014, *ApJ*, 794, 107
- Rich, R. M., Corsi, C. E., Cacciari, C., et al. 2005, *AJ*, 129, 2670
- Riess, A. G., Casertano, S., Yuan, W., et al. 2018, *ApJ*, 861, 126
- Saha, A., & Vivas, A. K. 2017, *AJ*, 154, 231
- Sandage, A., & Tammann, G. A. 1968, *ApJ*, 151, 531
- Schlegel, D. J., Finkbeiner, D. P., & Davis, M. 1998, *ApJ*, 500, 525
- Sesar, B., Fouesneau, M., Price-Whelan, A. M., et al. 2017, *ApJ*, 838, 107
- Sesar, B., Ivezić, Ž., Stuart, J. S., et al. 2013, *AJ*, 146, 21
- Shapley, H. 1953, *PNAS*, 39, 349
- Smolec, R., Pietrzyński, G., Graczyk, D., et al. 2013, *MNRAS*, 428, 3034
- Sneden, C., Preston, G. W., Chadid, M., & Adamów, M. 2017, *ApJ*, 848, 68
- Sollima, A., Borissova, J., Catelan, M., et al. 2006, *ApJL*, 640, L43
- Sollima, A., Cacciari, C., Arkharov, A. A. H., et al. 2008, *MNRAS*, 384, 1583
- Stellingwerf, R. F. 1982a, *ApJ*, 262, 339
- Stellingwerf, R. F. 1982b, *ApJ*, 262, 330
- Stetson, P. B., Braga, V. F., Dall’Ora, M., et al. 2014, *PASP*, 126, 521
- Tammann, G. A., Sandage, A., & Reindl, B. 2003, *A&A*, 404, 423
- Thompson, I. B., Kaluzny, J., Pych, W., et al. 2001, *AJ*, 121, 3089
- Vivas, A. K., Saha, A., Olsen, K., et al. 2017, *AJ*, 154, 85
- Welch, D. L., Wieland, F., McAlary, C. W., et al. 1983, *JRASC*, 77, 261
- Weldrake, D. T. F., Sackett, P. D., & Bridges, T. J. 2007, *AJ*, 133, 1447
- Zinn, J. C., Pinsonneault, M. H., Huber, D., & Stello, D. 2018, arXiv:1805.02650
- Zinn, R., & West, M. J. 1984, *ApJS*, 55, 45